

A Review of Tunable Inductors for Power Electronics: Techniques and Applications

Raheem Elsayed A. Azim Attia ^{a,*}, MIEEE

^a Department of Electrical Power Systems and Machines, Zagazig University, Zagazig, Al-Sharqiyyah, 44519, Egypt

*Corresponding author:

Raheem Elsayed,
Research Assistant,
Department of Electrical Power Systems and Machines,
Zagazig University,
Zagazig, Al-Sharqiyyah, 44519, Egypt
Mobile no.: +201021099108
Email address: raheemelsayed1@gmail.com

Word count (excluding abstract and references): 18,000

Number of Tables: 1

Number of Figures: 32

Number of References: 151

A Review of Tunable Inductors for Power Electronics: Techniques and Applications

Abstract—Magnetic components are recently being researched and believed to be a main source of losses, and increasing the weight of power converters, which has become a real challenge for designers. Controlled magnetics for power electronic applications is a promising but still-evolving technology that started to gain momentum as it enabled circuit designers to achieve greater optimization in terms of cost, losses, and size during the design stages of different power converters. In this paper, a comprehensive review is carried out on practical tunable magnetic technologies that may turn out to be a viable solution and find their usage in power electronic applications. In addition, several techniques that can be used in the realization of controlled magnetic components, including but not limited to current-controlled magnetics, voltage-controlled magnetics, and self-regulated magnetics, are being investigated to define the merits and drawbacks of each technology for potential future usage. This article is mainly focused on controlled power inductors for various power electronic applications, and its main goal is to assist designers in selecting the suitable technology for their applications.

Index Terms—Tunable magnetics, voltage-controlled magnetics, current controlled magnetics, self-regulated magnetics, variable power inductors, power electronic applications.

1. INTRODUCTION

Magnetic components, either energy-transfer devices such as transformers or energy-storage devices such as inductors, are crucial elements and a prominent part of any power electronic circuit [1]. Inductors play different vital roles in power electronic circuits, such as being used as energy-storage devices to serve different operating modes; being used as filters for switched current waveforms; and being used in snubber circuits to limit current change rate and transient currents. On the other hand, transformers are also not less important than inductors, and they play major roles that can be stated as transforming voltage levels that may be required for circuit operation; providing electrical isolation between different components in the circuit as a matter of safety; and matching impedance between different circuits to achieve maximum power [2, 3].

The study of power losses in magnetic components such as inductors and transformers is becoming more popular as it is one of the main elements that contribute greatly to the efficiency and stability of power electronic converters [4, 5]. These losses typically comprise of copper losses that take place in the copper wire winding as well as iron losses that are being dissipated in the iron core and are mainly caused by eddy currents, the hysteresis of the magnetization curve, and residual magnetism [6-8]. According to power loss analysis in [9], [10], [11], [12], and [13], the most dissipated power in these proposed power electronic converters occurs in magnetic components, whether transformers or inductors, rather than other losses such as conduction and switching losses of the power semiconductor devices. The proposed converters in [7] and [14] have only one inductor and one transformer respectively, at the same time, these topologies include many other power semiconductor switches. Taking into consideration the small number of magnetic components in these two converters as compared to other components and looking into power loss analysis in both cases, it can be noted that losses that occur in magnetic components are significant, although not dominant. Without losing generality, it can be stated that reducing magnetic component losses will contribute greatly to the converter's efficiency regardless of whether these losses occurring in the magnetic components are dominant as stated in [9-13] or not, as stated in [7] and [14], because even in the case that they are not dominant, they are still significant.

In addition to the loss problem, magnetic components such as power inductors still present a challenge in terms of size. The fact that most bulky components in power electronic converters are magnetic components is understood, as the magnetic core is most likely made of heavy iron to avoid saturation and the winding is mostly made of thick copper to reduce resistance and hence losses. These two reasons are behind the increase in the magnetic component's volume and weight. To compromise for loss and size issues, the design of magnetic components is usually the result of a trade-off between various variables such as size, efficiency, cost, inductance, direct current resistance, switching frequency, and saturation current [15, 16].

A promising solution for size and loss problems occurring in power converters can be controlled or tunable magnetics, that is, the ability to provide power inductors whose inductance can be varied while being in use, or similarly to provide transformers whose coupling coefficient, turns ratio, leakage, and magnetization inductances can be tuned online [17]. In power inductors used in DC-DC converters, it has been demonstrated that the power losses in these converters depend on the inductor's current, and there is an optimum value for the inductor's current that can improve the converter's efficiency. The inductor current needs to be changed independently from the load current, and this can be achieved using controlled magnetics [18, 19]. For instance, in power electronic converters proposed in [16], [20], [21], and [22], controlling the inductance of the main converters reduced the ripple current flowing through their inductors, which resulted in the following optimizations: 1) reducing the losses occurring in magnetic components to significant values and hence increasing the converter's efficiency; 2) reducing the size of the converter; and 3) improving the performance of the converter.

The discussion in this paper will be limited to tunable inductors, also known as variable inductors (VIs), and future research may focus on variable transformers (VTs) instead. Thus, this paper is dedicated to techniques and technologies that can be utilized to

dynamically control the inductance of power inductors online. In the rest of this article, various techniques and configurations that can be utilized to create controlled magnetic components for both current-controlled and voltage-controlled types will be investigated, stating the advantages and disadvantages of each technique. Later, power electronic applications utilizing tunable magnetics based on these technologies will be thoroughly examined, along with the advantages and drawbacks of each application, followed by future research suggestions to overcome these limitations. And finally, a conclusion will be presented.

2. CONCEPT OF MAGNETIC CIRCUITS

Magnetic materials are broadly classified into diamagnetic materials, paramagnetic materials, and ferromagnetic materials. Diamagnetic and paramagnetic materials have very low relative permeability approaching unity as compared to ferromagnetic materials. A further classification of ferromagnetic materials in terms of the hysteresis loop is soft magnetic materials and hard magnetic materials. The former is characterized by its narrow hysteresis loop; however, the latter is characterized by its wide hysteresis loop. In terms of power electronic applications, ferromagnetic materials, especially the soft magnetic ones, represent the ideal choice when designing magnetic components [23, 24].

A generic magnetic circuit with an air gap is depicted in Fig. 1. The physical design of this circuit may resemble a power inductor that is being extensively used in power electronic applications. In that circuit, the main winding consists of N turns, and it is being wound on a magnetic core with an air gap that shall be constructed of any soft magnetic material with a considerably high relative permeability of μ_r . The mean length of the magnetic core and the air gap is denoted by l_c and l_g , respectively. The effective cross-sectional areas of the magnetic core A_c and air-gap A_g are equal and are denoted by A .

When current denoted by i flows through the inductor's winding, it will produce a magnetic flux denoted by \emptyset , which will circulate confined within the magnetic core. It is typical to define magnetic flux intensity represented by H as provided in (1), where k is a constant equal to $N/(l_c+l_g)$. The magnetic flux intensity is directly proportional to the current, and it can be used instead of using current bearing in mind that increasing it means the current has increased. Similarly, it is common to define flux density in the core instead of magnetic flux; the magnetic flux density is denoted by B and is expressed simply as $B = \emptyset/A$, keeping in mind that magnetic flux density in the magnetic core is the same as in the air gap as the area of both are equal.

The relationship between the magnetic flux intensity H and the magnetic flux density B is given as simple as $B = \mu_0\mu_r H$, where μ_0 is the permeability of free space and is equal to $4\pi \times 10^{-7} \text{ H/m}$. For simplicity, the multiplication of relative permeability and free space permeability is called magnetic permeability and is denoted by μ . The relationship between magnetic flux density and magnetic flux intensity is commonly called the magnetization curve, or B-H curve [1, 2]. For instance, Fig. 2 illustrates the magnetization curve for a magnetic core made from silicon iron powder, a soft magnetic material [25]. The given B-H curve can be divided into two main regions, the linear region and the saturation region. Before the saturation of the magnetic core, the relation is linear, and in this linear region, it is typically clear that the magnetic permeability is constant and is equal to μ . The physical meaning of the linear region is simply that when current increases, the flux in the magnetic core increases linearly, maintaining a constant magnetic permeability. In contrast, in the saturation region, it is obvious that a further increase in current will only cause a very slight rise in the flux density, or, in other words, a very high current is required to generate a very low amount of flux. In saturation region, it is clear that the magnetic permeability is not constant anymore and it changes as current changes, implying that magnetic permeability is current-dependent, although the magnetic core material properties are not altered [26].

$$H = \frac{mmf}{l} = \frac{Ni}{l_c + l_g} = ki \quad (1)$$

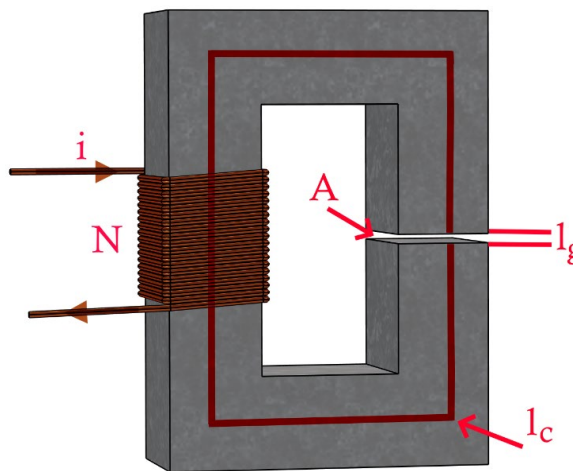


Fig. 1. Magnetic circuit with an air gap.

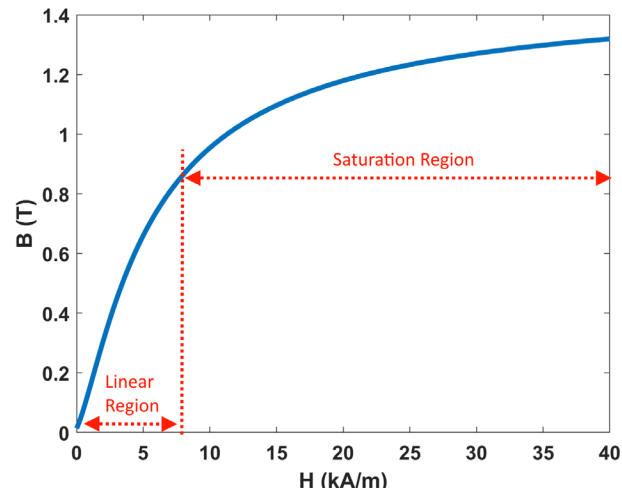


Fig. 2. Magnetization curve for silicon iron powder (FeSi) core.

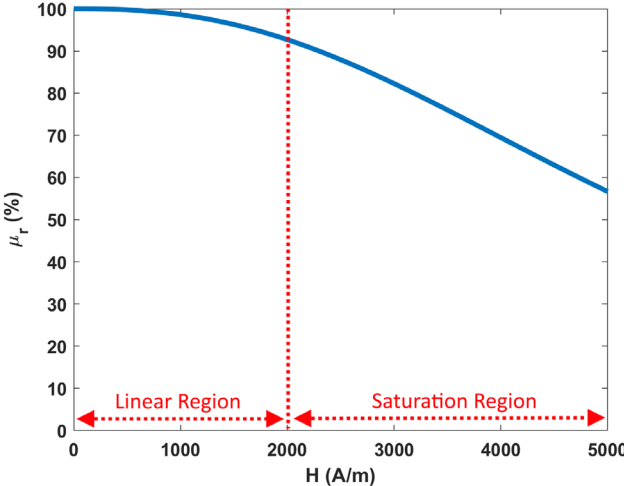


Fig. 3. Normalized relative permeability μ_r versus DC magnetization force H for silicon iron powder (FeSi) core.

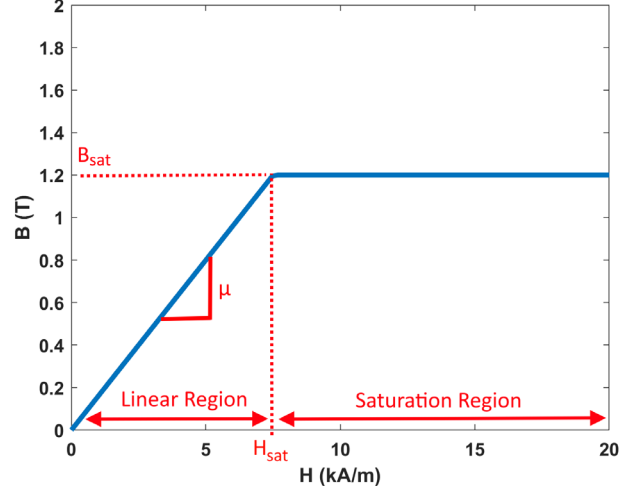


Fig. 4. Piece-wise linearized magnetization curve for silicon iron powder (FeSi) core.

The variation of percentage relative permeability, μ_r , against the magnetic field intensity, H , for a silicon iron alloy powder magnetic core is depicted in Fig. 3. The figure illustrates that the drop in permeability is not more than 10% during the linear region, indicating that it is nearly constant; however, in the saturation region, the permeability rolls off sharply to reach 60%, emphasizing the fact that the permeability is never a constant in the saturation region [25, 27]. For soft magnetic materials, it can be summarized that, in the linear region, the magnetic permeability of these materials is sufficiently high, constant, and current-independent; however, during saturation, the magnetic permeability decreases sharply and approaches zero, and it becomes current-dependent in that case.

The piece-wise linear model depicted in Fig. 4 significantly simplifies the magnetization curve of soft magnetic materials. The permeability before saturation in that figure is represented by the constant μ , while the permeability during saturation is zero. In this model, it is assumed that during the saturation of the magnetic core, the flux density will reach its maximum value, denoted by B_{sat} , and the flux density will no longer increase with an increment in current. B_{sat} is typically a constant that depends on the magnetic core material; it is the maximum that cannot be surpassed and is considered the upper limit that the peak flux density produced in the magnetic core should not exceed when designing magnetic components [1]. The saturation flux density of the most common soft magnetic materials is shown in Table I, and it is evident that the iron powder cores have a high saturation flux density and are much superior to ferrite cores, despite the fact that their relative permeability is much lower ($\mu_r < 200$) than that of ferrite cores [28, 29].

The insertion of an air gap in the depicted magnetic circuit in Fig. 1 produces a more linear magnetization curve, which enhances the current capability of inductors by increasing the current at which the core will saturate maintaining a constant permeability over wider range of currents, and this way the inductor can handle higher currents. Additionally, the core will have a higher energy storage capacity and won't be sensitive to potential fluctuations resulting in more stability. By including this air gap, a generic model for the inductance of power inductors can be developed, which will later be used to identify the techniques available for tuning inductance. The impact of the air gap on the B-H curve is clear in Fig. 5, where powder core with uniformly distributed air gaps is used. The air gap in ferrite materials is similar to that shown in Fig. 1, and there may be more than one gap distributed along the iron core. While, in powder cores, the air gap is uniformly distributed throughout the material, and these air gaps are created using a non-ferromagnetic material, insulating layer, that is being used to control the permeability of the core [2, 29-32].

According to the linearized reluctance model for magnetic circuits which assumes unsaturated magnetic core and uniform magnetic flux inside the magnetic core, the given circuit in Fig. 1 can be simply modeled as an MMF source with a value equal to Ni , where i is the current flowing through the winding and two reluctances connected in series; first reluctance represents the magnetic core, and the second one represents the air gap. The magnetic core reluctance denoted by \mathcal{R}_c and the air gap reluctance denoted by \mathcal{R}_g are given in (2) and (3), Fig. 6 illustrate the equivalent circuit [1].

TABLE I
SATURATION FLUX DENSITY OF TYPICAL CORE MATERIALS

Core Material	Saturation Flux Density (Tesla)
Ferrites	up to 0.45
Pure Iron Powder (Fe)	1.2 to 1.5
Nickel Iron Alloy Powder (NiFe)	up to 1.5
Silicon Iron Alloy Powder (SiFe)	up to 1.6

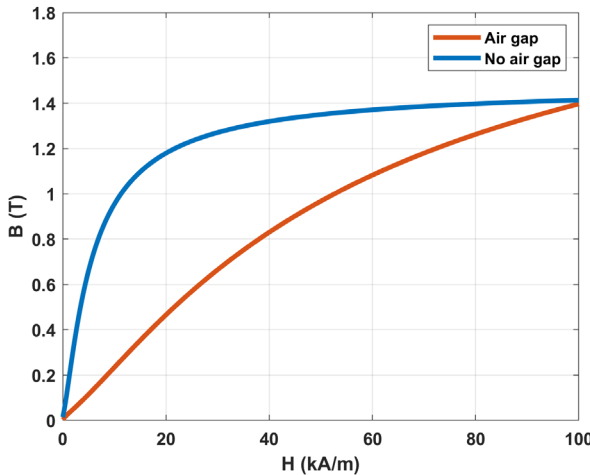


Fig. 5. Distributed air gaps effect on magnetization curve for silicon iron powder (FeSi) core.

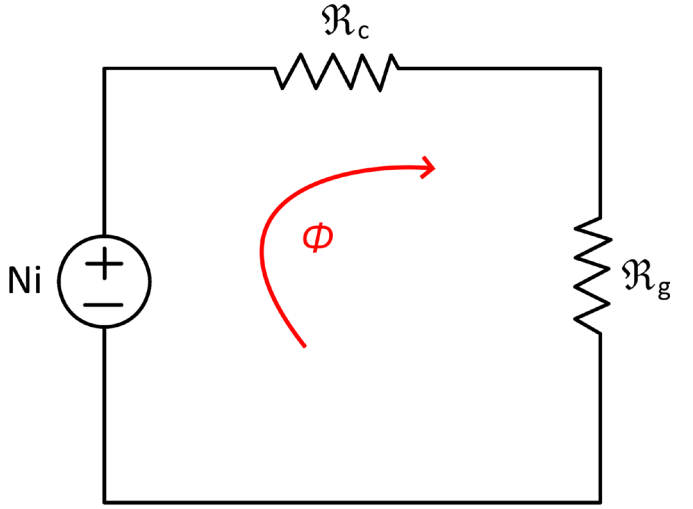


Fig. 6. Equivalent magnetic circuit model.

The overall reluctance of the air-gapped magnetic core denoted by \mathcal{R} is given in as $\mathcal{R} = \mathcal{R}_c + \mathcal{R}_g$, and the overall reluctance expression is presented in (4), noting that the following assumption was made $A_c = A_g = A$, neglecting the fringing flux effect. Since the magnetic reluctance the core provides depends on relative permeability, which is current-dependent in the saturation zone, it is not constant. According to the piece-wise linearized model, during the linear zone, the reluctance has a constant, definite low value (assumes high relative permeability), and it becomes infinite during saturation due to zero relative permeability.

The self-inductance of this magnetic circuit denoted by L can be calculated according to (5), and the final expression of self-inductance is given in (6). The significance of the inductance is how much energy that inductor can store, as the energy stored in an inductor in the time domain is directly proportional to the value of the inductance assuming constant current, given that the energy is $1/2Li^2$, where L is the inductance and i is the current flowing through the inductor. As long as the magnetic permeability is constant, which only happens in the linear portion of the magnetization curve, the inductance can be assumed to be current-independent. Otherwise, as the magnetic reluctance in the saturation region rises, the inductance will decrease and the magnetic core will be unable to store any more energy there [26].

The inductor must be designed so that it does not saturate at the maximum possible current; saturation can be a problem in terms of increasing losses and limiting the energy that inductors can handle. From the perspective of magnetic component design, it is ideal to have an inductor with a high inductance value and higher saturation current while at the same time maintaining a smaller size. On the other hand, in terms of power electronic applications, the inductance value must be chosen in a way that enhances the converters' overall performance, including their overall size, efficiency, transient response, and cost [15].

$$\mathcal{R}_c = \frac{l_c}{\mu_0 \mu_r A_c} \quad (2)$$

$$\mathcal{R}_g = \frac{l_g}{\mu_0 A_g} \quad (3)$$

$$\mathcal{R} = \frac{l}{\mu_0 A} \left(\frac{l_c}{\mu_r} + l_g \right) \quad (4)$$

$$L = \frac{N\emptyset}{i} = \frac{N^2}{\mathcal{R}} = \frac{N^2}{\mathcal{R}_c + \mathcal{R}_g} \quad (5)$$

$$L = \mu_0 N^2 A \left(\frac{l}{(l_c/\mu_r) + l_g} \right) \quad (6)$$

3. TECHNIQUES FOR TUNING INDUCTANCE

The inductance of a power inductor was given in (6); since the inductance value is solely dependent on the physical construction parameters of the winding and the magnetic core and independent of other variables such as current, assuming constant permeability. Therefore, the following techniques can be used to dynamically adjust the inductance value online for power inductors with construction similar to those in Fig. 1: 1) the number of turns the main winding N ; 2) the air gap size, shape and position l_g ; 3) core material which translates to the relative permeability of the magnetic core μ_r ; and 4) the inductor's overall shape, which can alter the magnetic core mean length l_c [22].

3.1 Number of Turns Technique

The number of turns can be varied with discrete steps or continuously to tune inductance online; in power electronic applications, the latter is preferred in order to achieve controllability over a greater range smoothly. According to (6), if other parameters remain constant, the inductance appears to be proportional to the square number of turns. This implies that raising or lowering the inductance of power inductors online and continuously can be achieved, typically by increasing or decreasing the number of turns, respectively. Additionally, since inductance is proportional to the square of the number of turns, any variation in the number of turns will have a significant impact on inductance as compared to other parameters, allowing for greater tunability as compared to other techniques stated earlier [33]. The major drawbacks of that method are: 1) Referring to (1), the magnetic flux intensity is proportional to the number of turns, which means that increasing the number of turns will result in a higher magnetic flux intensity for the same current value; thus, the core will saturate at lower currents, which will effectively lower the current-carrying capability of the power inductor; 2) increasing the number of turns can significantly increase the copper losses as the length of the conductor increases [26]. Although power electronic converters do not currently utilize discrete inductance control except in very rare applications, such as in [34], since it does not provide the complete control range needed to properly optimize these converters, the technology is available and has been presented in [34], [35], and [36]. The switches used can be either solid-state-based such as in [34], or mechanical based such as in [35] and [36].

3.1.1 MEMS-Based Configurations

For instance, the basic design of a two-step tunable inductor proposed in [35] is shown in Fig. 7. By simply varying the inductor's number of turns between two and four, the inductance value can be changed online, achieving two different values. Micro-electrical-mechanical-system (MEMS) technology is used in the proposed tunable inductor, enabling the integration of the whole design into a single chip. The inductor consists of a multi-turn spiral inductor and two electrostatic switches (MEMS switches), which may be switched on or off by applying a DC voltage across them. The electrostatic switches can be used to select between 2 and 4 turns of the multi-turn spiral inductor by simply bypassing a specific number of turns, which consequently will vary the inductance correspondingly to two distinct values. Thanks to MEMS technology, this configuration has two main advantages: 1) smaller sizes (micro level) of the whole inductor, including switching; and 2) low power consumption for the MEMS switches, which result in not affecting the overall efficiency of the applications [37, 38]. On the other hand, this configuration has two main drawbacks: 1) MEMS technology has not yet demonstrated its viability for high-power applications, which are typically the case in power electronic applications; and 2) the control of inductance is not continuous so limited and has only two options [39].

In contrast to discrete-steps variable inductors, continuous variable inductors have been introduced in [33], [40], [41], and [42] and are capable of continuously adjusting inductance by changing the number of turns online. These realized configurations vary in terms of the technology used; the first two are based on MEMS technology, while the latter is based on solid-state technologies. For instance, the basic design of a MEMS-based liquid-based continuous variable spiral inductor is illustrated in Fig. 8, which is based on concepts presented in [33] and [40]. This variable inductor consists of a tank that holds conductive metallic liquid, a micro-pump that controls the amount of liquid being injected, micro-pipes to transfer the liquid to the channel, a spiral inductor consisting of four turns, and a channel where the liquid will be injected, and that channel is in direct contact with the inductor turns. Normally, the present current path is approximately 4 turns before injecting any liquid, as given in Fig. 8. On the other hand, when the conductive liquid is injected into the channel, the liquid comes into contact with the coil turns. This reduces the effective current path by bypassing portions of the coil turns and consequently reducing the number of turns, as illustrated in Fig. 9. By doing so, the inductance of that inductor can be varied continuously online. The main advantages of such a configuration are: 1) that the whole inductor and all its components are integrated into one chip, resulting in a smaller size thanks to MEMS technology; 2) that high efficiency is achieved due to the use of micro-pumps that consume less power; and most importantly, 3) that inductance can be continuously tuned online. However, this configuration is still facing the same problems as stated earlier, as the MEMS technology is not yet proven in high-power applications.

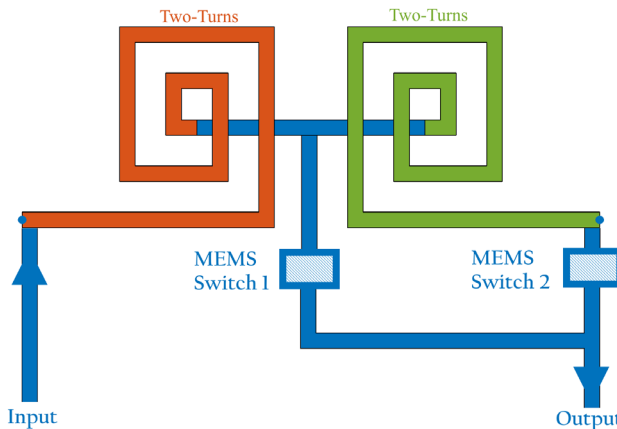


Fig. 7. Two-steps MEMS-based variable inductor.

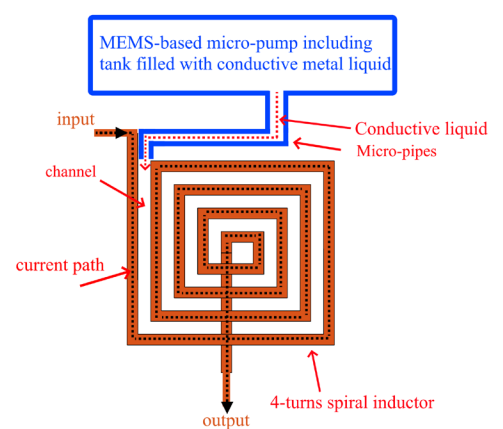


Fig. 8. MEMS-based liquid-based continuous variable spiral inductor design.

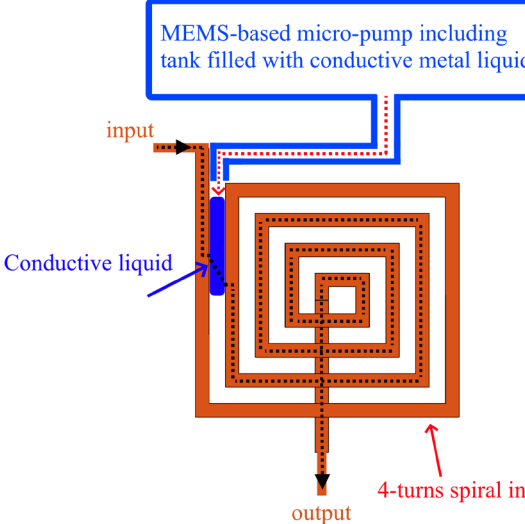


Fig. 9. MEMS-based liquid-based continuous variable spiral inductor operation.

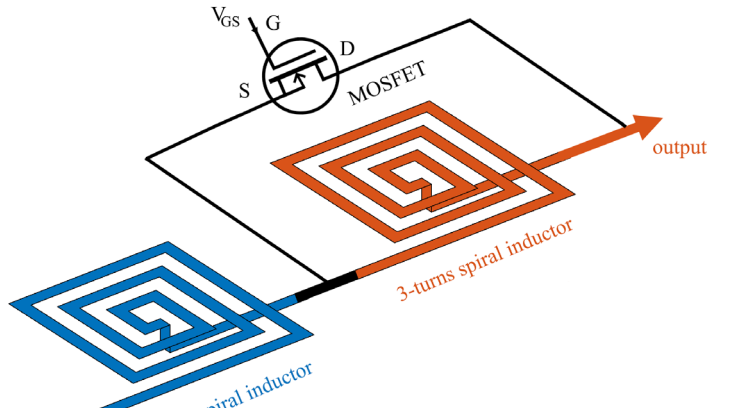


Fig. 10. Solid-state-based voltage-controlled tunable inductor configuration.

3.1.2 Solid-State-Based Configurations

A solid-state-based variable inductor that partially depends on changing inductance by physically altering the number of turns is depicted in Fig. 10. This basic configuration consists mainly of two spiral inductors connected in series and a MOSFET switch connected in parallel with one of them; all of them are integrated into a single microchip [40]. The parasitic impedance of the MOSFET, which is usually dominated by the parasitic drain-to-source resistance (R_{DS}), can be changed by controlling the gate-to-source control voltage (V_{GS}) of the MOSFET. When the control voltage (V_{GS}) is zero, the impedance offered by the MOSFET from drain-to-source is extremely high and can be regarded as an open circuit. As the control voltage increases, however, the impedance begins to decline until it reaches its minimum value at a sufficient control voltage, which can be considered a short circuit [43]. The operation is simply given as, when the MOSFET is in off-state, it acts as an open circuit; the number of turns will be a maximum of six, and hence the inductance will be maximum. On the other hand, when the MOSFET is in on-state, it acts as a short circuit, and three turns are bypassed, so the overall number of turns in that case is a minimum of three, and hence the inductance will be minimal. Although, in on/off cases, the inductance is changed by physically altering the number of turns, to change the inductance between minimum and maximum values, another idea is utilized. The number of turns will not be altered physically; however, the impedance of the MOSFET will be controlled via controlling voltage (V_{GS}) between open-circuit and short-circuit conditions in order to change the overall impedance seen by the input source, thereby modifying the overall effective inductance. The key merits of this configuration are that: 1) it can be made smaller and more compact; 2) it can be implemented for power electronic applications as power MOSFETs are capable of handling high power effectively; and 3) a high tunability range can be achieved. On the other side, the main drawback of this configuration that makes it impractical will be the increased conduction losses due to the high drain-to-source resistance (R_{DS}) of the MOSFET required to achieve higher values of inductance, which can significantly reduce the overall efficiency of any power electronic converter.

3.2 Air-Gap Length Technique

The inductance of a power inductance can be tuned continuously online by varying the air gap length of ferromagnetic as well as iron powder cores. Inductance is also affected by the geometry and position of the air gap; typically, the optimal geometry, either a constant air gap, a stepped air gap, or a sloped air gap, is chosen based on the application [44, 45]. Once the inductor is constructed, the geometry and position of the air gap are fixed, and only the air gap length may be altered online by mechanical methods to tune the inductance. The inductor's inductance provided in (5) can be approximated by noting that for ferromagnetic cores, the relative permeability is of high value in comparison to the permeability of free space, $\mu_r \gg \mu_0$. It implies that the magnetic core reluctance is significantly lower than the air gap reluctance, $\mathcal{R}_c \ll \mathcal{R}_g$, and that the core reluctance can be neglected when taking the air gap reluctance into consideration. This results in a reduction of the inductance expression to (7), noting that the fringing effect is neglected [46].

$$L = \frac{N^2}{\mathcal{R}_g} = \frac{\mu_0 N^2 A_g}{l_g} \quad (7)$$

According to (7), the inductance is inversely proportional to the air gap length, meaning that a higher air gap length results in a lower inductance value and vice versa. The significant correlation between inductance and air gap is the reason for the wide tunability range of inductance when using this method. This technique may also be applied to iron powder cores because, in addition to the distributed air gaps that are present in iron powder cores, additional concentrated air gaps that can be variable are inserted in such cores to further increase the saturation level of the core [47-49]. Although the fringing effect was neglected, larger

air gap lengths can significantly increase it. This can lead to greater losses in the magnetic core and winding as well as increased vibration because of the concentrated electromagnetic force in the air gap area. To minimize the fringing effect and reduce vibration behavior, this technique will employ several air gaps; however, this can lead to a bigger magnetic core, greater manufacturing technical difficulties, and an increase in the total cost of the inductor [30, 50, 51]. Additionally, a mechanical means is employed to adjust the air gap, which significantly has a negative effect on response time. Furthermore, the area of the air gap and its position should be selected in a manner to minimize the fringing effect at the design phase [52].

3.2.1 Mechanically-Controlled Configurations

The fundamental design for this technique is depicted in Fig. 11. It comprises two ferromagnetic U-shaped cores, one of which is fixed and the other of which is free to move. The inductor's main winding is wound around the fixed core, while an actuator employs a control motor, such as a servo or stepper motor, attached to the movable core. The actuator and motor, in particular, are designed to handle extreme magnetic forces while the heavy ferrite core is in motion. As the control motor increases the air gap length, the inductance will drop until it reaches a static constant value. The variation of inductance with air gap length is plotted in Fig. 12. Rather than using the approximated model from (7), the exact model provided in (6) is employed in the plot. The following assumptions are made to plot this graph, the number of turns $N = 100$, the area $A = 100 \text{ mm}^2$, the core is made of ferrite with relative permeability $\mu_r = 2000$, the core mean length l_c assumed to be 100 mm, and the air gap maximum variation length is assumed to be 25 mm, while the minimum length is 1 mm. The inductance clearly decreases rapidly with air gap length between 1 and 10 mm, and then it appears to have reached a steady value; no significant change happens to inductance with a change in the air-gap length; this behavior is confirmed by practical measurements in [53]. The non-linear inductance variation is consistent with the simplification assumed in (7), in which the inductance is inversely proportional to the length of the air gap. This technique's primary benefit is its ability to achieve a high tunability range, yet its drawbacks may be summarized as follows: 1) low response time due to mechanical means used to control bulky movable cores; 2) increased losses in mechanical actuators and motors owing to heavy mass moment of inertia; 3) the production of multiple air gap cores to reduce the fringing effect is more expensive and technically difficult; and 4) limited to small power applications due to increased electromechanical forces. The disadvantages of this technique outweigh its merits, which makes it unsuitable for practical power electronic applications and limited to laboratory work unless further modifications are made [17, 53].

An enhanced modified design utilizing an air gap length variation to tune the inductance online is illustrated in Fig. 13. It consists of a fixed ferrite core and a free-moving air-core inductor attached to a movement control mechanism. The movement control mechanism comprises an actuator and a control motor, such as a servomotor. The air-core inductor's mass moment of inertia is much lower than the heavy iron core's; therefore, moving the lighter inductor requires a lower control motor rating. Consequently, the actuator and the control motor will be less expensive and dissipate lower losses, suggesting that this design is a viable option for medium- and high-power converters. The air-core inductor has a number of turns represented by N and a length indicated by l_c , while the ferrite core length is twice as long as the inductor and has a width equal to its thickness equal to b . The relative permeability and cross-sectional area of the ferrite core are expressed by μ_r and A_c , respectively, noting that the latter equals b^2 . The concept of operation is as follows: the inductance is maximal when the air gap length, represented by l_g , is zero, which happens when the core is completely within the air-core inductor. As the ferrite core gets farther away from the air-core coil, the air gap length, l_g , increases and the inductance decreases. When $l_g=l_c$, as depicted in Fig. 13, the inductance is minimal in this case, and the ferrite core is completely outside the air-core inductor. The inductance for this design as a function of air-gap length is given in (8), considering that this is the only variable. When substituting $l_g=0$, the inductance expression given in (8) simplifies to (9), which is referred to as the maximum inductance and is denoted by L_{\max} ; in contrast, the formula reduces to (10) when substituting $l_g=l_c$, and this is referred to as the minimum inductance and is represented by L_{\min} . Based on the equation given in (8), the variation of inductance with air gap length is plotted in Fig. 14. The following assumptions are made to plot this graph, the number of turns $N = 10$, the area $A = 100 \text{ mm}^2$, the core is made of ferrite with relative permeability $\mu_r = 1000$, the inductor's mean length l_c assumed to be 100 mm, and the air gap maximum variation length is assumed to be equal to $l_c/2$, while the minimum length is zero. It is evident that the inductance decreases linearly as the air gap length increases, which is consistent with the practical results presented in [54]. The benefits of this design can be summarized as: 1) a broad range of achievable inductances; 2) faster response due to the lower mass moment of inertia of the mechanical movement system; 3) reduced losses in the mechanical system owing to the lower mass moment of inertia; and 4) cost-effectiveness since the moving system's cost decreased drastically. With all of these merits, power electronic converters used in wireless power transfer (WPT) methods are a good use case for this design [54]. The primary drawback of this design is its size; it is not compact due to the necessity of a longer ferrite core than the air-core inductor for reliability purposes. In addition, due to the continuous movement, the wear out of the mechanical moving parts is another critical concern. The use of MEMS technology, as suggested in [55], can address these problems; nevertheless, it has not yet been proven that medium- or high-power converters may benefit from such a realization.

$$L = \mu_0 N^2 A_c \left(\frac{\mu_r \left(1 - \frac{l_g}{l_c}\right)^2}{l_c - l_g} + \frac{l_g}{l_c^2} \right) \quad (8)$$

$$L_{\max} = \frac{\mu_r \mu_0 N^2 A_c}{l_c} \quad (9)$$

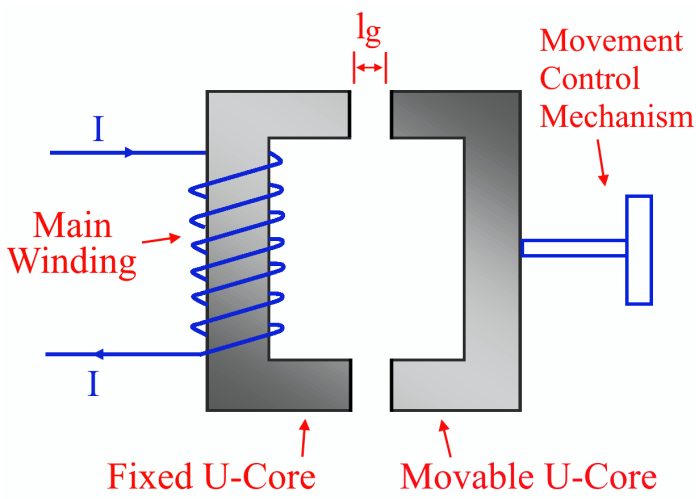


Fig. 11. Schematic diagram of the basic design of a ferrite double U-core air-gapped variable inductor.

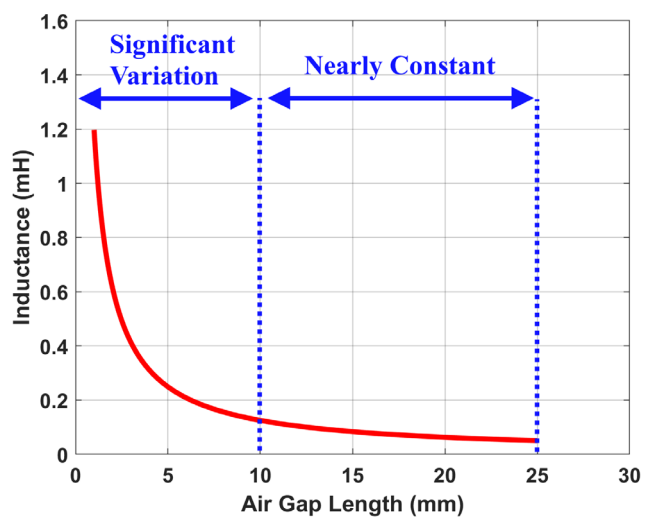


Fig. 12. Variation in inductance with air gap length of a basic ferrite double U-core air-gapped variable inductor.

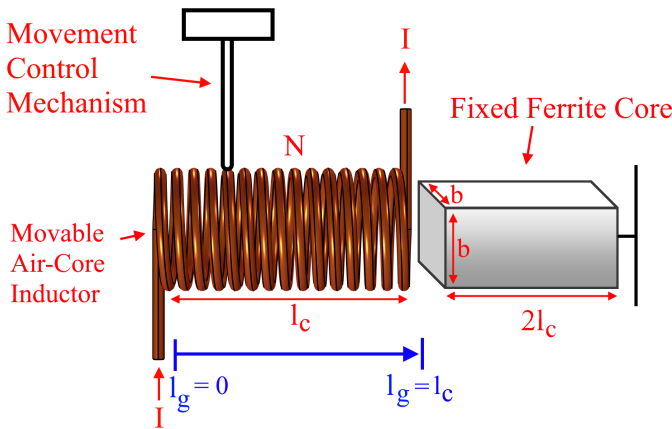


Fig. 13. Schematic diagram of the improved design of the variable air gap length inductor.

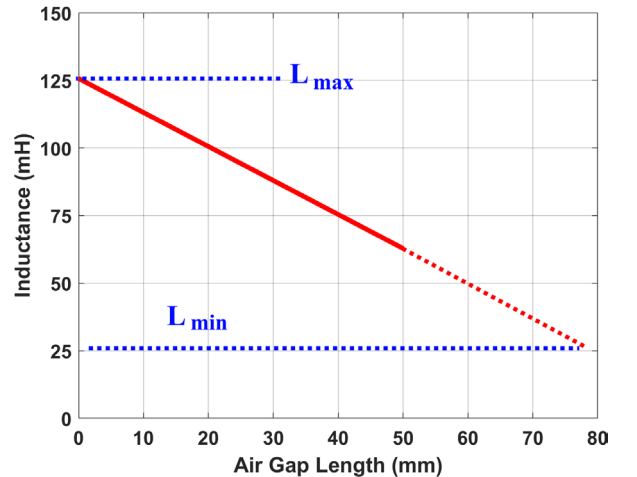


Fig. 14. Variation in inductance with air gap length of the enhanced variable air gap inductor.

3.2.2 Current-Controlled Configurations

The air-gap-changing approach necessitates the elimination of mechanical movement control systems in order to reduce overall size and response time. The virtual air-gap (VAG) technique is able to create virtually air-gaps with any desired gap length with the aid of a DC bias control current. This approach is promising for medium- and high-power converters, especially resonant converters. Additionally, its usage can be extended to reactive power compensation, harmonic filtering, and other power system-related applications. Different configurations for the realization of this technique have been proposed in previous literature, such as in [56-67].

The fundamental configurations of virtual air-gap techniques utilized in variable inductors are depicted in Fig. 15. The U-core and toroidal core configurations are illustrated in Figs. 15a and Fig. 15b, respectively. This basic design, either U-core or toroidal core configuration, comprises two magnetic cores interconnected together in an orthogonal manner and two windings wound around these cores. The main winding is wound around the main core, and these winding terminals represent the inductor's terminals, while the auxiliary or control winding is wound around the auxiliary core. In order to minimize or eliminate the induced emf and harmonics caused by the main winding on the auxiliary winding, orthogonal biasing is employed, in which the two working fluxes that result from the main and auxiliary windings, respectively, must be perpendicular to each other [68]. The orthogonal biasing is achieved by installing the two magnetic cores orthogonally. During the manufacturing process of the two cores, an unintentionally fixed actual air gap might be created, which should be minimized if not completely eliminated. The insertion of a small air gap can increase the inductance's tunability range and extend the inductor's power range [59]. On the other hand, a larger air gap can have a negative impact on the inductance tunability range, resulting in a reduced range [58]. The two cores can either be constructed of the same material or different materials, depending on the requirements of the application. For instance, a high-

permeability main core connected with a low-permeability auxiliary core, or alternatively, a high-permeability two-core configuration, yields a high tunability range, and the inductance of the main winding is highly independent of load current [56, 60]. The principle of operation of this technique is that the main flux generated by the AC main winding circulates in the main core, while the control flux produced by the DC auxiliary winding circulates in the auxiliary core. The two fluxes interact in the shared volume between the main and the auxiliary core, and the degree of saturation of the shared volume is being adjusted by controlling the DC bias current flowing through the auxiliary winding. For instance, a higher DC bias current causes the shared volume to become more saturated, increasing the reluctance of this portion of the core. Controlling the degree of the locally saturated volume of the magnetic core is similar to creating an air gap and controlling its length. In fact, the length of the virtual air gap can be translated into a real mechanical length, which is being controlled by controlling the DC bias current [69]. For a higher degree of tunability for the virtual air-gap length and hence the inductor's inductance, a high DC bias magnetization force is required; moreover, larger and multiple shared volumes are necessary. The inductance variation with DC bias current is similar to the inductance variation with air gap length given in Fig. 12. As demonstrated by the practical measurements provided in [58, 60, 67], the inductance varies in an inverse non-linear manner; initially, an increase in DC bias current will result in a sharp drop in the inductance, and subsequent increases in the DC bias current will cause an insignificant decrease in the inductance. The copper losses in the auxiliary winding are equal to the square of the auxiliary winding's DC bias current multiplied by the resistance of the auxiliary winding. Instead of raising the auxiliary winding DC bias current to increase the DC magnetization force because the losses are directly proportional to the squared number of the DC bias current, increasing the number of turns of the auxiliary winding can increase the DC magnetization force without contributing considerably to the overall losses since it is directly proportional to the value of resistance. Furthermore, when the shared volume between the main and auxiliary cores increases, a wider range for the virtual air gap length may be accomplished, increasing the degree of freedom in inductance tuning [56, 58].

The equivalent reluctance model of the proposed technique is shown in Fig. 16, where, N_m is the main winding number of turns, i_m is the main winding AC current, N_a is the auxiliary winding number of turns, i_a is the auxiliary winding DC bias current, \emptyset_m is the flux produced by main winding and flowing in the main winding, \emptyset_a is the flux produced by auxiliary winding, R_m is the reluctance of the main core, R_g is the parasitic air-gap reluctance, R_a is the reluctance of auxiliary winding, $R_{m,sv}$ is the reluctance of the shared volume between the main and auxiliary cores. The parasitic air-gap reluctance is part of the main winding equivalent circuit since it is assumed that the main core has been cut, while on the other hand, the auxiliary core is not cut. This parasitic air-gap reluctance can be minimized by using an enhanced manufacturing process rather than cutting the cores manually. The main core equivalent circuit additionally includes the shared volume's reluctance since variations in this volume's reluctance affect the main core circuit's total reluctance and, consequently, the inductance value of the main inductor [56, 57, 61].

Further enhanced configurations that imply multiple shared volumes, or, in other terms, multiple virtual air gaps, are depicted in Fig. 17. Fig. 17.a and Fig. 17.b illustrate the U-core configuration and the torrid core configuration, respectively. A novel design for the virtual air gap technique is illustrated in Fig. 17a. In this optimized configuration, the main AC winding is divided into two halves and connected in series to form the main winding, and similarly, the auxiliary winding is divided into two halves and connected in series to form the auxiliary winding. This configuration size is the same as the configuration proposed in Fig. 15; however, in this design, there are two virtual air gaps instead of one. As the number of virtual air gaps increases to two while the core's overall size remains constant, the inductance tunability range expands, allowing for more flexibility in the variation of the main inductor's inductance. A setup like this requires less space and materials than the one shown in Fig. 15a, assuming the same inductance tunability range. In addition, the tunability range for the system shown in Fig. 17a may be further expanded by adding more control cores if necessary [58]. The design presented in Fig. 17b employs three control cores, which can create three virtual air gaps of controllable length. This design outperforms the one described in Fig. 15b in terms of inductance tunability range, size, and efficiency. In general, the purpose of adding several control cores is to increase the number of virtual air gaps and, as a result, expand the main winding inductance's tunability range. Furthermore, efficiency, compactness, and tunability range may all be improved with more control cores, and the number of control cores can be chosen depending on the requirements of the application [56]. The advantages of this method may be summed up as follows: 1) a wide range of inductance tunability is easily achievable; and 2) it has an extremely rapid response as compared to other designs that use air gap length to alter inductance. However, there might be certain drawbacks: 1) the difficulty of manufacturing such special core configurations may result in higher overall costs; 2) increased losses in auxiliary winding may cause a significant drop in overall efficiency; and 3) certain designs, as given in Fig. 15, may have larger overall sizes due to low material and space utilization factors. As previously mentioned, the losses issue may be handled by increasing the auxiliary winding's number of turns. Alternatively, control windings can be made of specific superconducting materials that have a very low resistance at low temperatures and hence enhance the current that can be carried by control windings to achieve higher mmf without increasing total losses [62, 66]. Furthermore, the low utilization problem can be overcome by innovative configurations, as provided in Fig. 17.

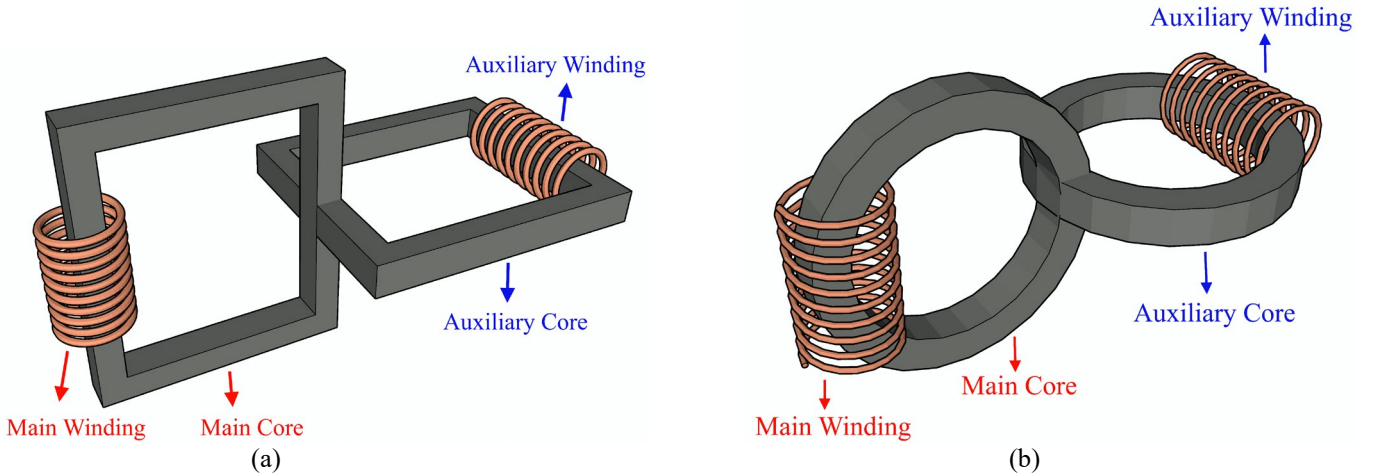


Fig. 15. The basic structure of a virtual air gap variable inductor. (a) U-core configuration; (b) Toroidal core configuration.

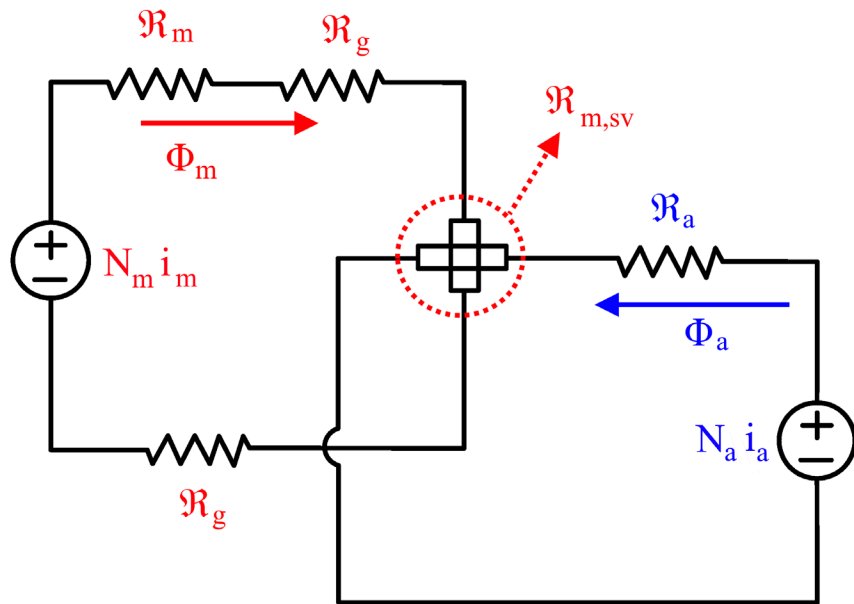


Fig. 16. Equivalent magnetic circuit model of a basic virtual air gap variable inductor.

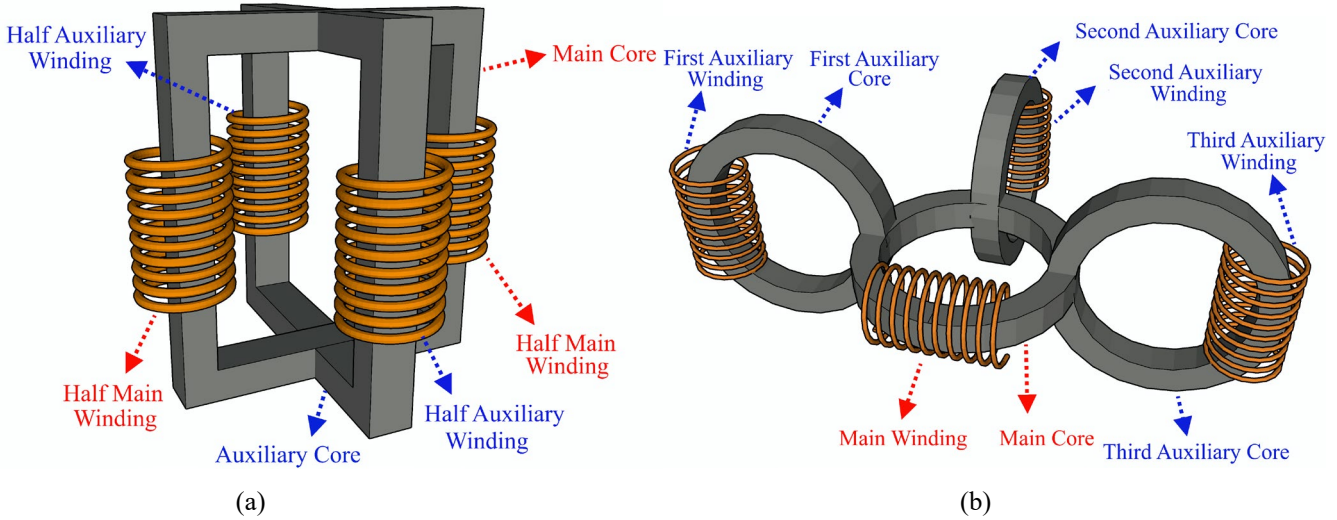


Fig. 17. The structure of an enhanced virtual air gap variable inductor. (a) U-core configuration; (b) Toroidal core configuration.

3.3 Relative Permeability Technique

Controlling the relative permeability, μ_r , as given in (6) is one of the most effective techniques to regulate inductance online. Referring to Fig. 3, relative permeability appears to be independent of current during the linear region and is dependent on the magnetic core material only; on the other hand, relative permeability is clearly dependent on current during saturation, and it starts to decrease as the magnetic core saturates. That change in relative permeability can be exploited in order to tune the inductance online. There are three main approaches utilized to control the relative permeability of magnetic cores: 1) current-controlled approach, and it is the most popular one that utilizes an external DC bias current to adjust the relative permeability of the magnetic core; 2) liquid-controlled approach, and it is the less popular approach that employs MEMS technology in conjunction with liquid fluids to alter the relative permeability of the medium, which represents the magnetic core in that case; 3) voltage-controlled approach, still-evolving technology that employs an external DC bias voltage to adjust the relative permeability of the magnetic core. The first technique is DC current bias, also known as actively current-controlled variable inductors, and is the most frequently utilized in power electronic converters, as discussed in [16], [20], [21], [22], [70], [71], [72], [73], [74], [75], [76], [77] and [78]. While, the second and third approaches are less popular in power electronic applications.

3.3.1 Current-Controlled Configurations

The basic design of a current-controlled variable inductors can be divided into two main configurations: double toroidal and double E-core. The schematic diagram of the former design is shown in Fig. 18, while the design of the latter is shown in Fig. 19. Both configurations function on the same operational principle, which is to alter the relative permeability of the magnetic core with the aid of an external DC bias current in order to adjust its inductance. The external DC bias current is typically controlled by an auxiliary converter, which is usually a non-inverting buck converter. These configurations employ parallel biasing, in which the two fluxes of the main and auxiliary winding are in parallel, either additive or subtractive. Parallel biasing often alters the relative permeability of the entire magnetic core, allowing for a wider inductance tuning range. However, the main disadvantage of this biasing scheme is the formation of unintended magnetic coupling between the main and auxiliary windings, which can induce unwanted emf in the auxiliary winding, negatively affecting the control circuit and even reflecting effects on the main winding by increasing harmonics in it. The undesired magnetic coupling effect is generally avoided by wounding both windings in such a way that any induced emf cancels out [64, 68].

Referring to the double toroidal core variable inductor configuration depicted in Fig. 18, it is comprised of two sets of windings, referred to as the main winding and the auxiliary winding, wound around two toroidal cores that are magnetically decoupled. The main winding represents the two terminals of the variable inductor, and the auxiliary winding serves as the control winding that can be used to control the magnetic core permeability and, consequently, the inductance of the main winding. The main winding number of turns is denoted by N_m , and it is split into two equal portions wound around each of the two toroidal cores. In a similar manner, the auxiliary winding has a number of turns denoted by N_a and is also divided into two equal sections wound around each of the two toroidal cores. The main winding carries the main AC current denoted by I_m , which produces a magnetic flux denoted by Φ_m . Meanwhile, the auxiliary winding carries a small DC control current denoted by I_a , which generates a magnetic flux denoted by Φ_a . The auxiliary winding, in comparison to the main winding, is a low-power winding capable of handling small DC control currents, is built of smaller cross-sectional area conductors, and has a high number of turns. Such a design is utilized to reduce losses in the auxiliary winding so that they do not have a substantial impact on the inductor's overall efficiency, and the high number of turns will compensate for the small DC control current, resulting in considerable MMF for permeability control. The auxiliary winding is wound in a manner to ensure that the following conditions are met: first, the auxiliary winding flux either cancels out a portion of the main flux or reinforces the main flux in both cores in order to control the degree of core saturation, and thus the inductor's inductance is controlled; and second, the mutual coupling effect between the main and auxiliary windings is zeroed out in order to eliminate any transformed voltage due to the main winding on the auxiliary winding. Depending on the direction of the DC bias current I_a , the total flux in that toroidal cores can be either additive or subtractive. This means that the saturation level can be raised in the case of additive fluxes and lowered in the case of subtractive fluxes. As discussed earlier, as the inductor is driven into saturation, the relative permeability begins to decrease, which causes the inductance to decrease as well. This is how inductance is adjusted in such a scheme: the flux produced from the auxiliary winding will cancel out a portion of the main winding flux, reducing the saturation level, increasing relative permeability, and ultimately increasing inductance. On the other hand, when the main winding's flux is reinforced by the auxiliary winding's flux, the saturation level will rise, decreasing the permeability and therefore the inductance. There are several benefits to using two toroidal cores and splitting the primary and auxiliary windings evenly: 1) raise the inductor's saturation level to allow for higher operating currents; 2) allow for bidirectional operation while reducing the mutual coupling effect between the main and auxiliary windings, so that the mutual transformed voltage at the auxiliary winding is canceling rather than being additive regardless of the direction of the main winding current; and 3) allow for reducing a portion of the main flux or increasing the main flux in order to control the degree of saturation and hence the inductor's inductance in a more flexible way. The double toroidal configuration has demonstrated its effectiveness in bidirectional DC-DC converters, particularly in applications where saturation of the core is commonly anticipated and control of the degree of saturation is essential [20-22, 73, 74].

The schematic design of the double E-core current-controlled variable inductor is depicted in Fig. 19. This E-core structure is composed of two E-cores layered on top of one another and has three magnetic legs, with the central leg air-gapped. The main winding, which functions as the inductor terminals, is wound around the middle leg, while the auxiliary or control winding is

divided into two equal sections and is wound around the right and left arms. The technical parameters of the main and auxiliary windings are similar to those of the double toroidal core configuration in terms of the number of turns and cross-section area. In order to eliminate the mutually-induced voltage that occurs from the main winding on the auxiliary winding, the auxiliary winding is divided into two equal portions and connected in series in opposite polarity. Similar to the double toroidal core design, the principle of operation of this configuration is as follows: when an AC current flows through the main winding, represented by I_m , it generates a flux Φ_m , which will circulate in the magnetic core's center, right, and left arms. In contrast, when the DC control current passes through the auxiliary winding, which is denoted by I_a , it will produce a flux denoted by Φ_a , and that flux will only flow on the outer circumference of the magnetic core and will not flow through the central leg due to the air gap. The air gap introduced in the central leg makes the inductor less vulnerable to variations in the E-core's magnetic properties and enhances the core's saturation level. The E-core becomes increasingly saturated as the control current I_a increases, which reduces the magnetic core's relative permeability and, consequently, the inductor's inductance. The reluctance equivalent circuit for this configuration is depicted in Fig. 20. The reluctances of the left section of the magnetic core are represented by \mathcal{R}_{c1} , \mathcal{R}_{c2} , and \mathcal{R}_{c3} , and their summation is denoted by $\mathcal{R}_{c,left}$ as presented in (11). Similarly, the reluctances of the right section of the magnetic core are represented by \mathcal{R}_{c4} , \mathcal{R}_{c5} , and \mathcal{R}_{c6} , and their summation is denoted by $\mathcal{R}_{c,right}$ as given in (12). While \mathcal{R}_{c7} represents the central limb's core reluctance, \mathcal{R}_g represents the central limb's air gap reluctance, and their summation is indicated by $\mathcal{R}_{c,central}$ as illustrated in (13). The central leg reluctance $\mathcal{R}_{c,central}$ is considered to be uncontrolled since the auxiliary winding flux Φ_a is not circulating in that limb due to the existence of the air gap. On the other hand, the reluctances of the left and right sections of the magnetic core, represented by $\mathcal{R}_{c,left}$ and $\mathcal{R}_{c,right}$, are being controlled by the auxiliary winding DC bias current. The main and auxiliary fluxes are clearly additive in the left portion of the core and opposing in the right section. As the DC bias current increases, the relative permeability of the left section of the core drops, and therefore its reluctance, indicated by $\mathcal{R}_{c,left}$, increases. In contrast, when the DC bias current increases, the relative permeability of the right section of the magnetic core increases, and therefore the reluctance of this section, represented by $\mathcal{R}_{c,right}$, decreases. As a consequence of these non-uniform variations in relative permeability and reluctance of the magnetic core, the main winding inductance is affected. The typical relationship between the main inductor's inductance and the auxiliary winding DC bias current is illustrated in Fig. 21 [17, 25, 79-81]. The main inductor's inductance drops as the DC bias current of the auxiliary winding increases, indicating that the core is getting more saturated with increase in the DC bias current. Typically, this relationship is applicable for both the double toroidal core and the double E-core configurations. Several prototypes were built and tested as reported in [16, 20, 71-74, 76, 77, 79, 80, 82], and the main inductance as a function of DC bias current was found to be consistent with the relationship indicated in Fig. 21. In unidirectional DC-DC converters, like resonant converters, where power flows only in one direction, the double E-core configuration is commonly employed [20, 72, 75-79, 82, 83].

$$\mathcal{R}_{c,left} = \mathcal{R}_{c1} + \mathcal{R}_{c2} + \mathcal{R}_{c3} \quad (11)$$

$$\mathcal{R}_{c,right} = \mathcal{R}_{c4} + \mathcal{R}_{c5} + \mathcal{R}_{c6} \quad (12)$$

$$\mathcal{R}_{c,central} = \mathcal{R}_{c7} + \mathcal{R}_g \quad (13)$$

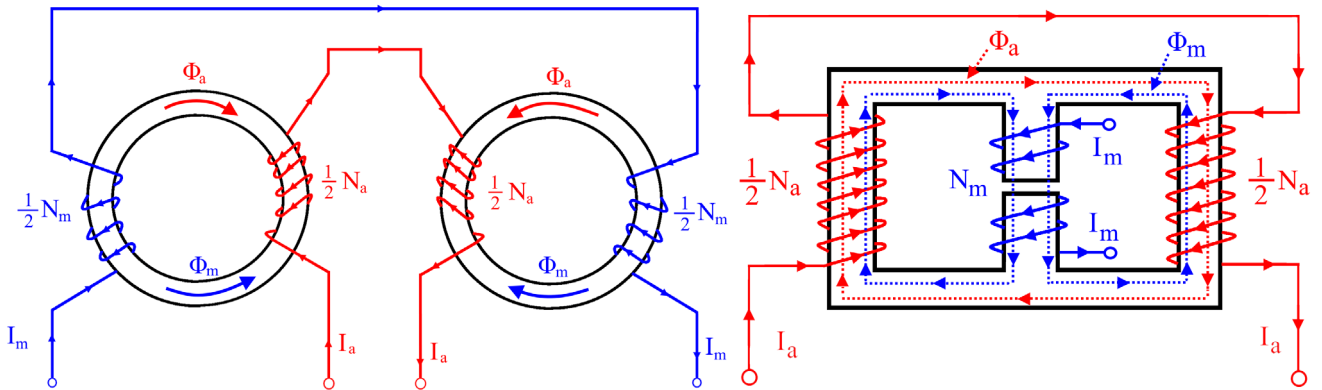


Fig. 18. Schematic diagram of double toroidal core variable-inductor configuration.

Fig. 19. Schematic diagram of double E-core variable-inductor configuration.

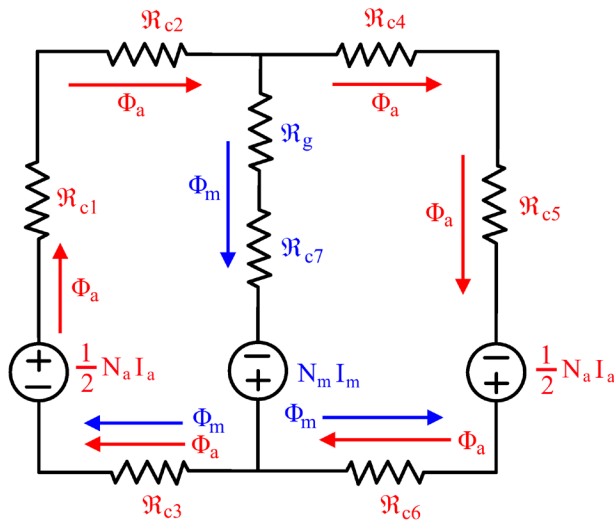


Fig. 20. Equivalent magnetic circuit model of double E-core variable-inductor configuration.

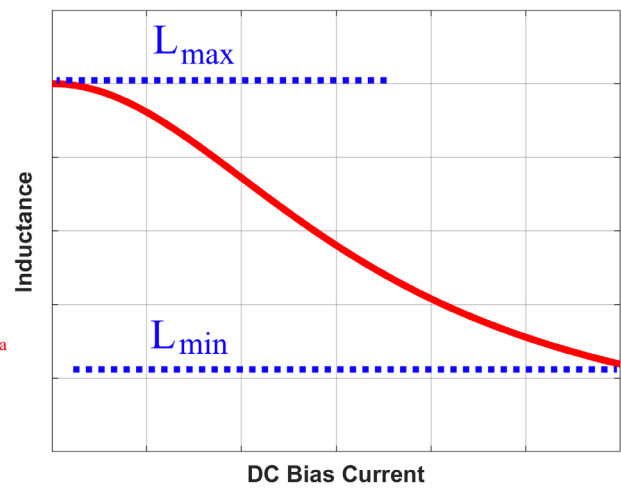


Fig. 21. The typical relationship between the main inductor's inductance and the auxiliary winding DC bias current.

3.3.2 MEMS-Based Configurations

The liquid-based MEMS variable inductor is the other technique that tunes the inductance online by altering relative permeability. The fundamental layout of this variable inductor is shown in Fig. 22. This form of inductor is a solenoid constructed of copper wire with a certain number of turns N . The current flowing through the solenoid is indicated by the letter I and the inductor is wound in a way that creates an empty channel that is by default filled with air or vacuum. A specified amount of saturated salted water is injected into the inductor's channel using micropipes and a micropump. By increasing the amount of injected salted water, the relative permeability increases, thereby increasing the inductance. The benefits of this approach include the ability to tune the inductance online continuously, the ability to achieve a wide range of inductances online, cost-effectiveness, increased efficiency, and simplicity of design. The primary drawback of this design, though, is that it is not as common in power electronic applications because of the low inductance values that can be acquired with it, making it impractical for high-power applications. However, this approach could be promising in the future as a result of advancements in MEMS technology [84].

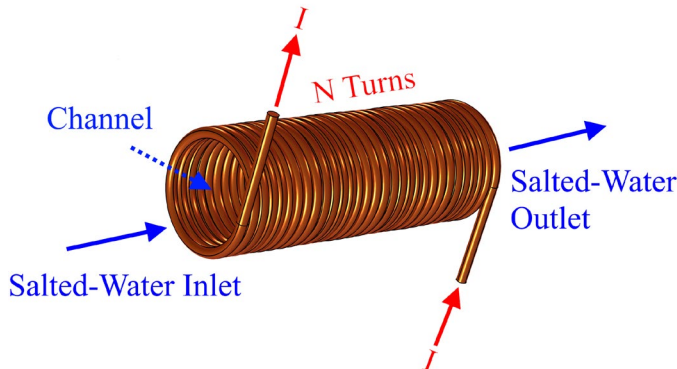


Fig. 22. Schematic diagram of liquid-based MEMS variable inductor.

3.3.3 Voltage-Controlled Configurations

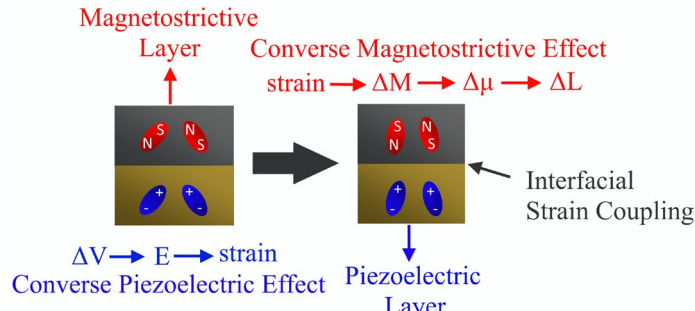


Fig. 23. The modulation mechanism of inductance for voltage-controlled variable inductors based on the converse magnetoelectric effect.

All of the techniques that have been covered thus far fall into the category of current-driven or current-controlled variable inductors, where the inductance value was adjusted online using a DC bias current. The increased losses and size are the common issues with all of these techniques. When considering an alternative to current-controlled variable inductors, voltage-controlled variable inductors based on the converse magnetoelectric (CME) effect can be a viable option. Magnetoelectric voltage-controlled variable inductors have demonstrated a high inductance tunability range, compactness, and low power consumption, which reduces losses [85-87]. Magnetoelectric composites utilized in voltage-controlled variable inductors are commonly made up of piezoelectric or ferroelectric and magnetostrictive or ferromagnetic materials in order to achieve strong converse magnetoelectric coupling. The strong inverse magnetoelectric coupling of the composites suggests a substantial ability to tune the magnetic characteristics of the ferromagnetic material by applying an external electric field to the ferroelectric material. Magnetoelectric voltage-controlled variable inductors (ME-VIs) operate on the strain-mediated magnetoelectric coupling concept as illustrated in Fig. 23. Applying an external constant electric field (E), generated by a DC voltage (ΔV), across the ferroelectric material induces strain within the ferromagnetic material; this is explained according to the inverse piezoelectric effect. Due to the strong strain-mediated ME coupling between the two materials, this generated strain is transferred to the ferromagnetic material through the interface between both materials, causing shape deformation in the ferromagnetic material. According to the inverse magnetostrictive effect also known as Villari effect, deformations in a ferromagnetic material will induce a magnetic field within the material, resulting in a change in the saturation magnetization (ΔM) of the ferromagnetic material, thereby altering the relative permeability ($\Delta \mu$) and, hence, the inductance (ΔL) of that material. This essentially means that the permeability and, consequently, the inductance of the ferromagnetic material can be controlled online for a core composed of a strong inverse magnetoelectric coupling composite by applying an external constant electric field to the ferroelectric material within the composite [86, 88-94].

The relation between relative permeability of the ferromagnetic material as a function of the mechanical stress applied on it is provided in (14), where $\mu_{r,f}$, M_s , K_0 , λ_s , and σ_f are the ferromagnetic layers relative permeability, the saturation magnetization, the initial magnetic anisotropy, the saturation magnetostriction constant, and the applied stress across the ferromagnetic material, respectively [86, 90, 95, 96]. The relative permeability of a ferromagnetic material varies depending on the saturation magnetostriction constant (λ_s) and the type of stress applied to it (σ_f). The majority of common materials employed in ferromagnetic layers have a saturation magnetostriction constant that is typically positive, $\lambda_s > 0$ [88]. Principally, the stress applied to the ferromagnetic material is transferred to it through the piezoelectric material. If the ferromagnetic material is subjected to compressive stress, implying that the applied stress is negative ($\sigma_f < 0$), then increasing the applied stress will cause the relative permeability of the ferromagnetic material to increase. On the contrary, when tensile stress is applied to ferromagnetic material, this indicates that the stress applied is positive ($\sigma_f > 0$); in this scenario, increasing the applied stress will cause the relative permeability to decrease. Consequently, as the relative permeability increases, the inductor's inductance will increase as well, and vice versa.

$$\mu_{r,f}(\sigma_f) = \frac{\mu_0 M_s^2}{2K_0 + 3\lambda_s \sigma_f} + 1 \quad (14)$$

When a constant electric field is applied across a ferroelectric material, it will deform, either compressive or tensile, depending on the effective piezoelectric coefficient and the polarity of the applied electric field. The stress exerted on the piezoelectric material denoted by σ_p is expressed simply as $\sigma_p = Y d_{eff} E$, where Y stands for Young's modulus, d_{eff} for the effective piezoelectric strain coefficient, and E for the applied electric field on the piezoelectric material [86, 90]. In the case of in-plane stress, the effective piezoelectric coefficient (d_{eff}) is computed as $(d_{31} - d_{33})/(1 + \nu)$, where d_{31} , d_{33} , and ν are the transverse constant, the longitudinal constant, and Poisson ratio, respectively [97]. The typical values of the most common piezoelectric materials show that the transverse piezoelectric coefficient (d_{31}) is negative and the longitudinal piezoelectric coefficient (d_{33}) is positive, implying that the effective piezoelectric coefficient (d_{eff}) is usually negative for these materials [88]. In case of longitudinal stress, the effective piezoelectric coefficient is equal to longitudinal piezoelectric coefficient (d_{31}), and as the longitudinal piezoelectric coefficient is typically negative, the effective piezoelectric coefficient is negative as well [96]. According to the piezoelectric stress formula (σ_p), a negative effective piezoelectric coefficient (d_{eff}) indicates that when a positive electric field is applied across the ferroelectric material, the applied stress will be negative, meaning that it is a compressive stress. However, the applied stress will be positive when a negative electric field is applied across the ferroelectric material, suggesting that the stress is tensile. The transferred stress from ferroelectric to ferromagnetic materials in the magnetoelectric composite is mainly dependent on the shape of both ferromagnetic and ferroelectric components. For instance, a magnetoelectric composite consists of two plates glued together, one of which is piezoelectric and the other ferromagnetic. It is assumed that the piezoelectric material has a negative effective piezoelectric coefficient and the ferromagnetic material has a positive saturation magnetostriction constant. The piezoelectric material will therefore experience compression upon the application of a positive electric field, which will be translated into tensile stress in the ferromagnetic material as if the ferromagnetic material is being dragged downward. Figures 25, 27, and 29 provide examples that fit into this explanation. However, with the same assumptions, if the shape is two rings placed inside each other such as in Fig. 28, compression in the piezoelectric material will result in compression in the ferroelectric material, and vice versa. This essentially indicates that the shape of the material plays a crucial role in determining how the applied electric field will affect the ferromagnetic material's relative permeability. Several designs for magnetoelectric voltage-controlled variable inductors have been published in previous works of literature [85, 87, 90, 98-103], with some of them proven in power electronic converters; the common designs are categorized into either plate-shape type, ring-shape type, or combination of them. Different configurations of these common designs will be discussed in the paragraphs that follow.

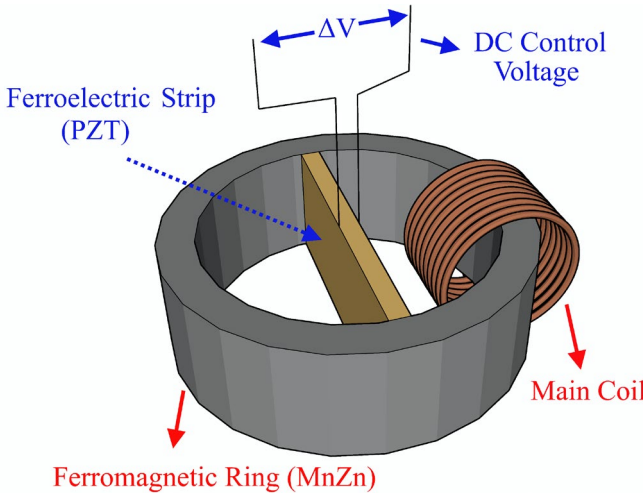


Fig. 24. The structure of a basic magnetoelectric voltage-controlled variable inductor.

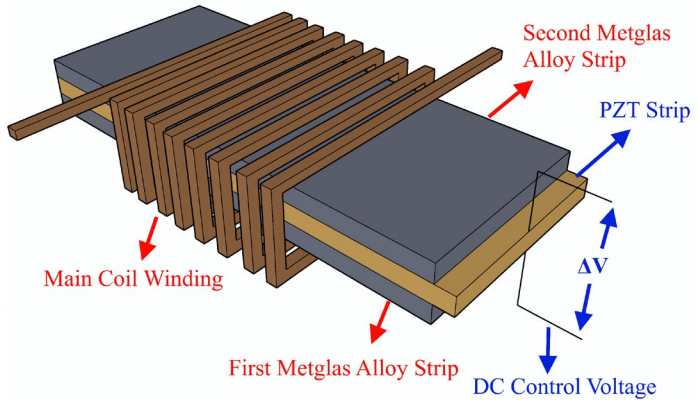


Fig. 25. The schematic construction of an improved magnetoelectric voltage-controlled variable inductor.

The construction of a fundamental design of a magnetoelectric voltage-controlled variable inductor is depicted in Fig. 24 [98]. It is composed of a piezoelectric strip, a magnetostrictive ring, and the inductor's coil. The ferroelectric strip is constructed of a solid solution of lead zirconate (PbZrO_3) and lead titanate (PbTiO_3), often known as $\text{Pb}(\text{Zr}, \text{Ti})\text{O}_3$ or simply PZT. The ferromagnetic ring is formed out of manganese zinc (MnZn) ferrite, which has a high relative permeability and typically high resistivity. The coil of the inductor, which is wound around the ferromagnetic ring, has N turns. The PZT ferroelectric strip is fitted tightly along the ring's diameter in a manner that guarantees their interfacial coupling to one another. It is worth mentioning that the proposed system's size is measured in millimeters; however, a higher power rating would imply larger dimensions. When a positive-polarity DC voltage is applied across the PZT strip, a constant electric field is formed along the strip, and the PZT strip shrinks in the direction of the applied field according to the inverse piezoelectric effect and due to the negative piezoelectric coefficient ($d_{31} < 0$). In contrast, the PZT strip expands in the direction of the applied electric field when a negative-polarity DC voltage is applied across it. The mechanical deformations, or induced strains, caused by the applied electric field on the PZT strip are subsequently transmitted to the ferromagnetic ring through their interfacial contact. As a result, the ferromagnetic ring undergoes mechanical deformations, which in turn induce a magnetic field inside the ring, resulting in changes in the ring's permeability and, consequently, the inductor's inductance. Typically, compressive stress in the PZT strip causes compressive stress across the ferromagnetic ring, and vice versa. This is mostly due to the applied electric field's direction, which is parallel to the PZT plate width. The practical results in [98] indicate that applying a DC voltage of 1 kV increases the inductance linearly, but reversing the polarity causes the inductance to drop linearly. In this design, the inductance change represented by ΔL is found to be directly proportional to the change in the DC applied voltage denoted by ΔV , $\Delta L \propto \Delta V$, indicating that the relationship is linear, assuming all other parameters are constant. The benefits of this design can be summarized as follows: 1) in terms of size, it is compact; 2) it is inexpensive; 3) in terms of manufacturing process complexity, it is easy to fabricate its layers; and 4) low power consumption at low frequencies. However, a number of problems with this design also arise: 1) a limited linear inductance tunability range of up to 20% at an operating frequency of 15 kHz and a DC control voltage of 1 kV; 2) the operational frequency bandwidth is limited due to increased iron losses in the magnetic core, imposing limitations when using it in power electronic applications; and 3) yet, it has not been demonstrated for high-power applications, which is almost the case in power converters. Further investigations are still required to be carried out for this composite to determine to what extent it is a feasible option for power electronic applications.

A magnetoelectric voltage-controlled variable inductor with an enhanced design is depicted in Fig. 25 [85]. The proposed design consists of three slabs that comprise the inductor's core, made out of the following materials and arranged in the following manner: ferromagnetic, piezoceramic, and ferromagnetic, respectively, as well as the main inductor coil. The piezoceramic slab is constructed of piezoceramic material, a modification of PZT, while the two ferromagnetic slabs are made of soft magnetic material, metallic glass alloy (FeBSiC), commonly known as Metglas alloy. The thickness of the slabs is measured in micrometers and millimeters for ferromagnetic and piezoceramic materials, respectively, implying a significantly reduced size. The principle of operation is similar to the previous configuration, and it is based on the strong strain-mediated magnetoelectric coupling between the slabs. The PZT strip is subjected to a DC control voltage ranging from 0 to 600 V, and Fig. 26 illustrates how inductance decreases non-linearly as the applied DC control voltage increases at a low operating frequency of 100 Hz, as reported in [85]. It should be noted that the inductance will increase rather than decrease if the DC control voltage supplied to the PZT strip is reversed in polarity. Since PZT has a negative piezoelectric coefficient, applying a positive DC electric field across it will compress it in the applied field's direction. In the direction of the applied voltage, that compressive strain will be transferred as a tensile stress to the two Metglas layers. As a consequence, both the relative permeability and the inductance drop. The action is reversed, and the stress

applied across the Metglas layers becomes compressive when the applied voltage has its polarity reversed, increasing permeability and hence inductance. A significant inductance tunability range of up to 450% at 100 Hz in Fig. 26 is evident, demonstrating how strongly the applied voltage affects the inductance of the Metglas slabs at low and medium frequencies. At a maximum voltage of 600 V, the inductance tunability was found to be 250% and 50% at 100 kHz and 5 MHz, respectively, which is extremely high when compared to the prior configuration shown in Fig. 24. There are several benefits to this proposed design: 1) the power consumption due to energy lost in the PZT slab, as well as, iron losses lost in the Metglas ribbons is minimal at moderate frequencies; 2) an ultimately high non-linear inductance tunability range can be achieved at a moderate operating frequency; 3) in terms of size, it is compact; 4) regarding the manufacturing process, it is easy to fabricate; and 5) it is low in cost. The main drawback is that the increased iron losses in the Metglas slabs caused by eddy currents at higher frequencies severely limit the tunability range and, hence, restrict its uses in high-frequency applications, which are most common in power electronic applications. Furthermore, the tunability range, while wide, is non-linear, implying unsmooth inductance control. Enhancements are made to this design to extend its tunability range at higher frequencies. The main issue is that off-the-shelf available Metglas ribbons have a minimum thickness that is regarded as relatively high, which causes significant eddy current losses at high frequencies. Laminating Metglas ribbons, or, in other terms, employing thinner Metglas ribbons rather than using one, is a novel technique reported in [100] for reducing eddy current loss at higher frequencies. Despite the additional production cost and complexity required to get thinner ribbons, it has been demonstrated that employing more laminations for the Metglas slabs improved the inductance tunability range at higher frequencies, which may be promising for power electronic converters. Furthermore, this concept proved to be practically feasible in magnetically coupled resonance wireless power transfer (MCR-WPT) systems. By adding additional coil winding to the construction described in Fig. 25, the mutual inductance between the two windings can be adjusted over a wide range. The mutual inductance's relatively wide tunability range allowed MCR-WPT systems to achieve higher transmission efficiency [99]. To guarantee the effectiveness of these plate-type designs in power electronic converters, further study is necessary.

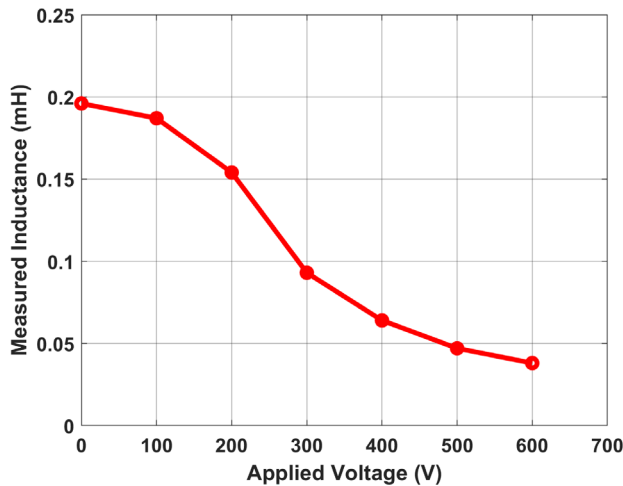


Fig. 26. The variation of inductance with applied voltage at a low frequency of 100 Hz.

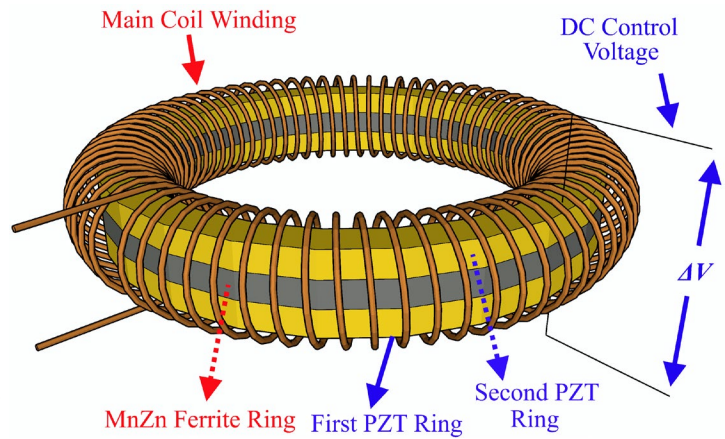


Fig. 27. The construction of a ring-type double piezoelectric layer magnetoelectric voltage-controlled variable inductor.

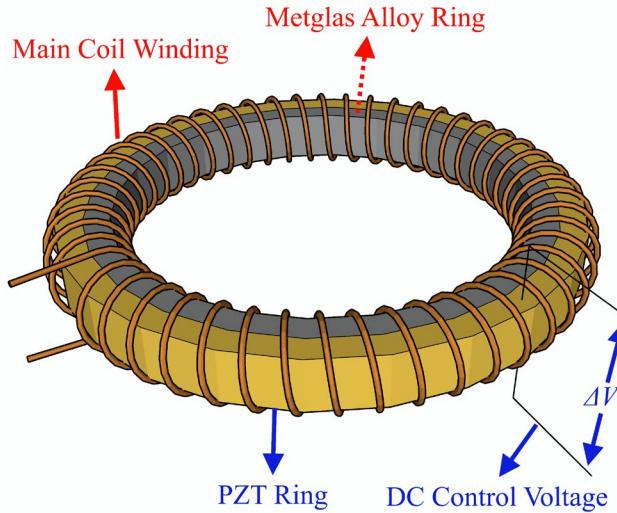


Fig. 28. The schematic design of a basic ring-type magnetoelectric voltage-controlled variable inductor.

In contrast to the design presented in [85], Fig. 27 illustrates the construction of a ME voltage-controlled variable inductor that uses two ferroelectric layers rather than two ferromagnetic layers [87]. The design consists of three rings arranged in the following manner to form the inductor's core, ferroelectric, ferromagnetic, and ferroelectric, as well as the inductor coil. The two ferroelectric rings are built of PZT, whereas the ferromagnetic ring is made of manganese zinc (MnZn) ferrite. The three rings are stacked on top of each other, as shown in Fig. 27, to guarantee strong interfacial contact between the core composites, and the inductor's coil is wound around them. Because of the strong strain-mediated ME coupling between the composites, induced stresses within the PZT layers caused by applying DC control voltage to those layers are transmitted to the ferrite layer, resulting in variations in the ferrite core permeability and thus the inductor's inductance. When a DC control voltage within the range of ± 300 V is applied to the two PZT rings, increasing the positive-polarity applied voltage results in a linear decrease in the inductance, while increasing the voltage in the opposite polarity, negative, causes the inductance to increase linearly, as reported in [87]. This design allows for a linear tunability range of up to 50% at low frequencies, such as 1 kHz, and up to 20% at high frequencies, such as 1 MHz, while the maximum tunability of 56.6% was obtained at 72 kHz, all is achieved at a low DC control voltage of 300 V. In comparison to the first and second designs, [98] and [85], this design can achieve a moderate linear tunability range at lower DC control voltages and moderate operating frequencies. A number of advantages can be concluded from this design: 1) a moderate linear inductance tunability range at moderate frequencies and electric fields; 2) the size of the proposed design is given in millimeters, indicating compactness; 3) ease of fabrication of the magnetoelectric composite; 4) low cost; and 5) reduced power losses as a result of lower electric field values that cause lower dielectric losses in the PZT material. Similar to previous configurations, a major disadvantage seems to be that the tunability range is limited with higher frequencies. In that aspect, it may not be suitable for power electronic converters, yet its linear inductance tunability behavior may be advantageous. This challenge, however, was overcome by adopting particular composites for the ferromagnetic layers that resulted in the elimination of magnetocrystalline anisotropy (MCA) and, thus, allowed for a wide inductance tunability range without experiencing excessive losses. The only difference between this novel design and the one illustrated in Fig. 27 is the materials that were employed. In that design, the ferromagnetic ring composite is constructed of two alloys: nickel-zinc-copper (NiZnCu) and cobalt ferrite (CoFe_2O_4), while the two ferroelectric rings composite are built of a mixture of lead magnesium niobite (PMN) and lead titanate (PT), widely known as PMN-PT. As a consequence, this suggested design was capable of achieving an extraordinary high tunability of up to 750% at a frequency of 10 MHz, as described in [102]. Further research is needed to validate the viability of these ring-type designs in medium- or high-power applications, which has yet to be demonstrated.

Another basic ring-type magnetoelectric voltage-controlled variable inductor design is depicted in Fig. 28 [101]. Likewise, to all previous configurations, it consists of two rings, ferromagnetic and ferroelectric, glued together, creating the core of the inductor, and the main inductor's coil is coiled around them. The ferroelectric ring is formed of PZT, whereas the ferromagnetic ring is composed of Metglas ribbons. The PZT ring was subjected to a DC control voltage ranging from -1 kV to 1.6 kV. The strong CME coupling between the materials forming the core caused the inductance to increase with a negative applied voltage and decrease with a positive applied voltage. In that regard, a linear inductance tunability range of up to 400% at a low frequency of 300 Hz and 1.6 kV was achievable, as described in [101]. Despite the fact that the tunability of the inductance is still achievable beyond this frequency over a very limited range, it is non-linear, implying that control is no longer smooth. Similar to the preceding configurations, the limited tunability range at high frequencies is caused by the Metglas ring's severe eddy current loss at higher frequencies. The key advantage of this arrangement is the simplicity of fabrication of the core, which can result in reduced cost because the design employs just two rings, in addition to lower dielectric losses and compactness. However, it is obvious that the inductance tunability range is very restricted to frequencies of only up to 10 kHz, making it unsuitable for power electronic applications. Reduced-thickness Metglas ribbons might significantly enhance the tunability range; however, as previously indicated, this would have a negative impact on total cost.

All preceding designs for ME voltage-controlled variable inductors have not been demonstrated to be suitable for high-power applications, and they are typically employed in low-power applications. To overcome that issue, the magnetic flux valve (MFV) concept has been introduced [103]. A ME voltage-controlled variable inductor based on the magnetic flux valve concept is realized by making a portion of the magnetic core of a magnetoelectric composite, and the reluctance of this part, commonly referred to as the magnetic flux valve, is controlled by varying the voltage applied to the piezoelectric layer of the magnetoelectric composite. This method's analogy thus far is comparable to the previously mentioned virtual air-gap approach, which controls the reluctance of specific magnetic core parts in order to control the magnetic core's total reluctance and, therefore, the inductor's inductance.

The design of a ME voltage-controlled variable inductor based on the magnetic flux valve principle is depicted in Fig. 29a. It comprises the main core, which is formed up of two U-shaped magnetic cores and one magnetic flux valve, in addition to the main inductor winding wound around the magnetic flux valve. The two U-shaped cores are composed of manganese zinc (MnZn) ferrite, and the magnetic flux valve that represents the center leg is built of a magnetoelectric composite. The magnetic flux valve is constructed from a predetermined number of ferroelectric and ferromagnetic layers stacked together using adhesives, as illustrated in Fig. 29b. The layers of the magnetic flux valve are layered on top of one another to ensure strong interfacial magnetoelectric coupling between these layers. Ferroelectric or piezoelectric layers are commonly formed of PZT, whereas ferromagnetic or magnetostrictive layers are produced of amorphous Metglas alloy. In fact, the two U-shaped ferrites are essential to ensure that the magnetic flux path is closed, thereby contributing to an overall increase in the tunability range of the inductance. To enhance the inductor's capacity for handling power while avoiding the magnetic core from quickly being saturated, a small fixed, intentional air gaps are placed between the two U-shaped cores and the magnetic flux valve. The wider the air-gap length, the higher the saturation current and hence the power capability that the inductor can handle; however, increasing the air-gap length reduces the

inductance tunability range, necessitating a trade-off between the inductance tunability range and the power capacity [90]. For that reason, four identical fixed air gaps are inserted between the right and left U-shaped ferrite cores and the magnetic flux valve, as depicted in Fig. 29a. The magnetic flux valve is made up of 22 PZT slabs and 44 Metglas ribbons that are placed one on top of the other; both have equal thicknesses in the millimeter range. Since the ferroelectric layers are comprised of non-magnetic material, the magnetic flux flowing through the magnetic flux valve will only pass through the ferromagnetic layers. As a result, the effective equivalent cross-sectional area of the magnetic flux valve limb is estimated using the number and thickness of ferromagnetic layers rather than ferroelectric layers. It is evident that there are twice as many ferromagnetic layers as there are ferroelectric ones. This results in a larger effective magnetic cross-sectional area for that limb; however, increasing the number of ferromagnetic layers causes increased eddy current loss and, therefore, a limited tunability range.

The magnetic reluctance model for this inductor is given in Fig. 29c, where the current flowing through the main winding is denoted by i , the number of turns in the main inductor's winding is indicated by N , the reluctance of the magnetic flux valve is denoted by \mathcal{R}_v , the reluctance of the four air gaps on the left and right U-shaped ferrite cores is equal and has a value denoted by \mathcal{R}_g , and similarly, the reluctance of the left and right U-shaped ferrite cores is equal and has a value denoted by \mathcal{R}_c . The main winding mmf is given as Ni , and it produces a total flux identified by \emptyset_t that flows essentially in the magnetic flux valve. It is then split into two components, \emptyset_1 and \emptyset_2 , flowing through the left and right U-shaped ferrite cores, respectively. The formula for inductance as a function of relative permeability of magnetic flux valve for that design is provided in (15). The mean length of ferromagnetic layers, air-gaps, and U-shaped ferrite cores is represented by l_f , l_g , and l_c , respectively; the effective cross-sectional area of ferromagnetic, piezoelectric, air-gaps, and U-shaped ferrite cores is denoted by A_f , A_p , A_g , and A_c , respectively, taking into consideration that $A_g = A_c$; the relative permeability of ferromagnetic layers and the ferrite U-shaped cores is indicated by $\mu_{r,f}$ and $\mu_{r,c}$, respectively; the number of ferromagnetic and piezoelectric layers in the magnetic flux valve is represented by n_f and n_p , respectively [90]. When a voltage between 0 and 400 V is applied to the PZT layers of the magnetic flux valve, the permeability of the Metglas layers $\mu_{r,f}$ decreases, increasing the reluctance of the magnetic flux valve limb R_v . This increases the overall reluctance of the magnetic path that is given by $R_v + R_g + R_c/2$ and consequently decreases the overall inductance of the inductor L , resulting in a maximum tunability range of up to 80% at power frequencies of either 50 or 60 Hz, as reported in [103].

$$L(\mu_{r,f}) = \frac{N^2}{\mathcal{R}_v + \mathcal{R}_g + \frac{\mathcal{R}_c}{2}} = \frac{N^2}{\frac{l_f}{n_f \mu_0 \mu_{r,f} A_f} + \frac{l_g}{\mu_0 A_g} + \frac{l_c}{2 \mu_0 \mu_{r,c} A_c}} \quad (15)$$

The key advantage of this approach thus far is that it can be employed in medium- and high-power applications, as opposed to all preceding configurations. The proposed design in [103], however, is limited to power frequencies and ignores the impact of increased eddy current losses in the Metglas ribbons at higher frequencies. Then, using it for power electronic applications could not be practical unless more stable ferrite materials used in the magnetic flux valve composite. Due to its frequency limitation, the Metglas-based MFV-based ME voltage-controlled variable inductors can be beneficial for a variety of power system applications, including, but not limited to, smooth reactive power compensation and voltage control in grids [104, 105]. A soft magnetic material with higher resistivity should be employed in the ferromagnetic layers of the magnetic flux valve to reduce eddy current losses and allow tuning of inductance at higher operating frequencies. Therefore, instead of Metglas alloy, the ferromagnetic layers will be composed of a nickel-zinc-copper (NiZnCu) and cobalt ferrite (CoFe_2O_4) alloy, while the ferroelectric layers and the two U-shaped ferrite cores will remain unchanged, formed out of PZT, and manganese zinc (MnZn) ferrite, respectively [90]. The U-cores and the magnetic flux valve are separated by four identical air gaps in order to improve the power handling capability, as stated earlier. The PZT layers inside the magnetic flux valve are subjected to a DC control voltage that ranges from 0 to 500 V. As the voltage was increased, the inductor's inductance decreased, and according to [90], inductance tunability of up to 220% at 1 MHz was achieved. This configuration offers several benefits, including: 1) a broad inductance tunability range at higher frequencies; 2) a viable solution for power electronic converters due to its ability to handle medium- and high-power; 3) minimized iron losses in the ferromagnetic slabs; 4) minimized dielectric losses in the PZT layers due to the fact that these layers' thicknesses can be significantly reduced through the use of multi-layer ceramic capacitor (MLCC) manufacturing technology, and hence the required DC control voltage is reduced substantially. The most significant drawback, meanwhile, could be the challenges in fabricating the magnetic flux valve, which might lead to an increased cost of the overall inductor. Furthermore, the structural problems associated with the ME composite design, such as the corner effect, have to be addressed by the use of unique designs; this might further complicate the manufacturing process, which adds to the main difficulty [106]. Yet, this configuration's ability to handle medium and high power at MHz operating frequencies with a wide inductance tunability range presents it as a potentially effective choice for power electronic applications.

In order to compare this design to the majority of other proposed designs, Table II summarizes the maximum inductance tunability for the most commonly proposed ME voltage-controlled variable inductors. The designs proposed in [102] and [90] are novel and promising because, in contrast to prior designs, they seem to achieve extraordinary linear inductance tunability ranges with high stability up to cutting-edge switching frequencies, which usually include the entire operating frequency range of state-of-the-art power electronic converters. In fact, the linear inductance tunability range emphasizes efficient and smooth inductance tunability over the non-linear ones. Bearing in mind that the inductance tunability, represented by γ , is determined by $(L_{max} - L_{min})/L_{min}$, where L_{max} and L_{min} represent the maximum and minimum achievable inductances at constant frequency under various applied electric fields, respectively. Furthermore, as stated earlier, the structure and shape of the piezoelectric and ferromagnetic materials, the materials used in the magnetoelectric composition, the range of the DC applied electric field, and the

fabrication process are all noticed to have an influence on the inductance tunability range of ME voltage-controlled variable inductors.

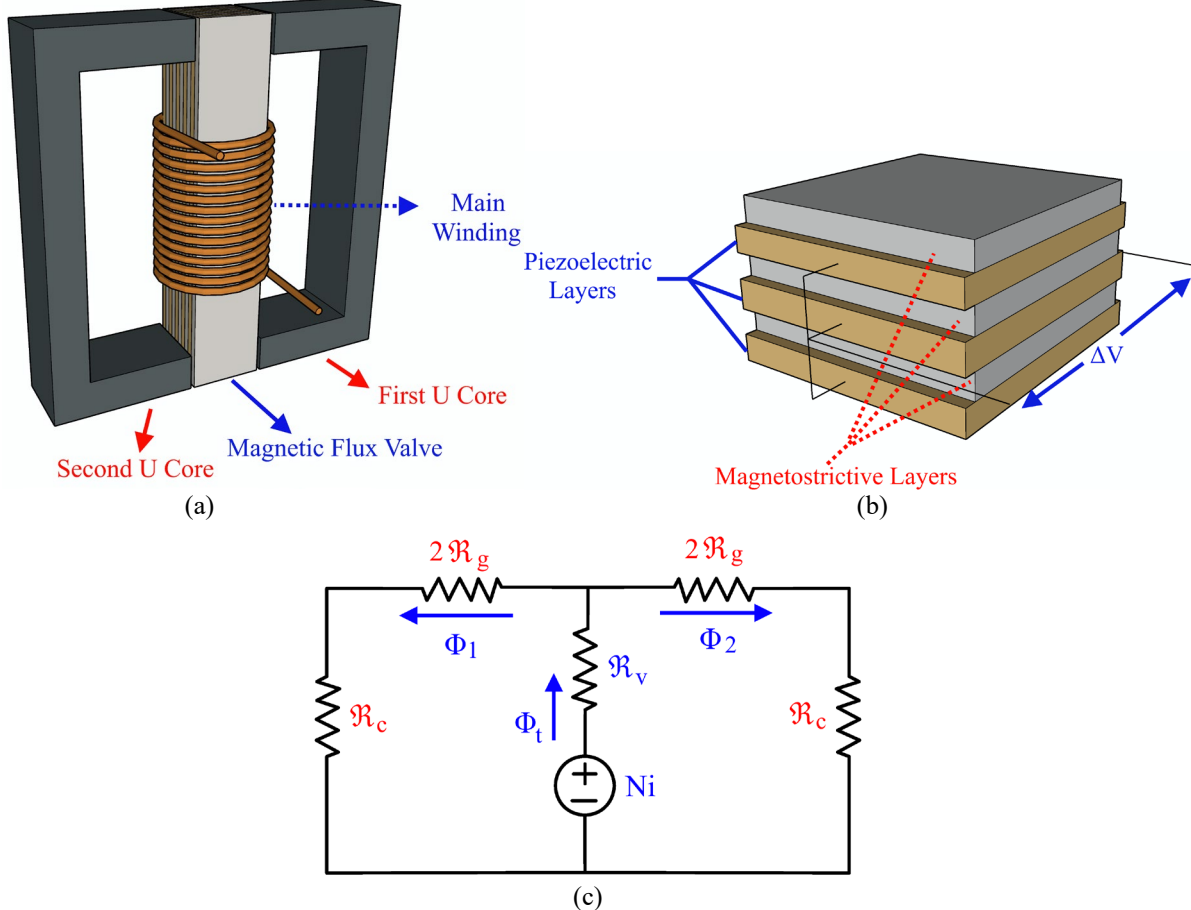


Fig. 29. MFV-based Variable Inductor. (a) The schematic structure of an MFV-based ME voltage-controlled variable inductor; (b) The schematic structure of a magnetic flux valve; (c) Equivalent magnetic circuit model of a basic MFV-based voltage-controlled inductor.

TABLE II
INDUCTANCE TUNABILITY RANGE OF MOST COMMON ME-VIS

#	ME Composite Material	Structure Shape	Inductance Tunability (%γ)	Electric Field (E)	Frequency	Ref.
1	MnZn ferrite/ PZT	Ring/Plate	20% - linear	5 kV/cm	15 kHz	[98]
2	Metglas/PZT/Metglas	Plate/Plate/Plate	450% - non-linear	12 kV/cm	0.1 kHz	[85]
3	PZT/MnZn ferrite/PZT	Ring/Ring/Ring	56.6% - linear	3 kV/cm	72 kHz	[87]
4	Metglas/PZT	Plate/Plate	250% - non-linear	5 kV/cm	1 kHz	[96]
5	Metglas/PZT/PZT	Plate/Plate/Plate	750% - non-linear	5 kV/cm	1 kHz	[96]
6	Metglas/PMN-PZT/Metglas	Plate/Plate/Plate	200% - non-linear	14 kV/cm	1 kHz	[86]
7	Metglas/PMN-PZT	Ring/Ring	1150% - non-linear	8 kV/cm	1 kHz	[86]
8	PMN-PZT/NiZnCu ferrite	Ring/Ring	16% - linear	8 kV/cm	6000 kHz	[86]
9	PMN-PT/(NiZnCu, CoFe ₂ O ₄) ferrite/PMN-PT	Ring/Ring/Ring	750% - non-linear	20 kV/cm	10,000 kHz	[102]
10	PZT/Metglas	Ring/Ring	412% - non-linear	16 kV/cm	0.3 kHz	[101]
11	PZT/(NiZnCu, CoFe ₂ O ₄) ferrite	Plate/Plate	220% - non-linear	20 kV/cm	5000 kHz	[90]
12	Metglas PZT/Metglas	Plate/Plate/Plate	56.5% - linear	16.7 kV/cm	30 kHz	[99]

4. APPLICATIONS AND FUTURE RESEARCH

4.1 Applications

Variable inductors have been employed in a variety of power electronic converter applications, mostly based on the previously stated techniques. Lighting drivers [70, 107-116], resonant converters [79, 80, 117-129], dual-active-bridge converters [72, 130, 131], wireless power transmission [54, 132-138], reactive power compensation and voltage control in power systems [139-141], and maximum power point tracking (MPPT) [142, 143] are all examples of applications that utilize the tuning inductance concept. Emphasizing the advantages and drawbacks of employing variable-inductance inductors in these converters is essential. Additionally, recommendations for further research that might address these drawbacks for possible applications in the future will be presented.

4.1.1 Lighting Drivers

Lighting drivers are essential in operating either discharge lamps or light-emitting diode (LED) lamps. Their most common use is to provide soft starting, safe operation, and smooth dimming control. Resonant inverters are typically utilized in discharge lamps that depend on electronic ballasts for operation. Electronic ballasts that are often used have dimming mechanisms that rely on either dc-link voltage control, switching duty-cycle control, or switching frequency control. The dc-link voltage control method maintains the inverter switching frequency and duty cycle constant while controlling the dc-link voltage by controlling the inverter's input dc voltage. In that manner, the lamp's voltage, current, and power can be adjusted by changing the dc-link voltage of the inverter. Although smoother linear dimming characteristics are produced by this simpler approach, soft starting cannot be accomplished with it, hence it is rarely employed. The average current and thus the power of the lamp can be adjusted when the duty cycle of the solid-state switches is changed while the dc-link voltage and switching frequency remain constant. However, this method may result in discontinuous drawn current at low lamp power and low duty cycles, and this discontinuous operation will increase electromagnetic interference and reduce the operation's reliability. As a consequence, increased stresses are noticed during discontinuous mode operation on solid-state switches, necessitating the need for additional protective circuits, such as snubber circuits, which may increase the total cost of this dimming technique. The switching frequency control technique involves altering the inverter's switching frequency while keeping the duty cycle and dc-link voltage constant, allowing for variations in the impedance of the resonant tank's series inductor, thereby controlling the drawn current and consequently regulating the lamp's power. Despite being straightforward, effective, and achieving soft starting, this method's dimming control is non-linear and unsmooth because of the high sensitivity of the lamp's power to the switching frequency [144-146]. It is possible to control the dimming without altering the dc-link voltage, the switching duty cycle, or the switching frequency, thus avoiding the disadvantages stated earlier by employing magnetically-controlled electronic ballasts, which use a variable inductor rather than a fixed one in the converter's resonant tank. This novel technique resulted in soft starting, linear dimming control, galvanic isolation between the control and power circuits, reduced overall cost, and increased efficiency over the entire dimming range [70, 82, 108-112, 145, 147].

The schematic design of a basic magnetically controlled electronic ballast driver is depicted in Fig. 30. It is composed of a half-bridge resonant inverter connected to a resonant tank. The auxiliary winding current, denoted by I_a , adjusts the resonant inductance, represented by L_r , to control the power supplied to the lamp. In short, changing the resonant inductance value (L_r) will alter the voltage that is applied to the lamp, which will change the current and power that it draws, consequently influencing the dimming of the lamp. The variable inductor used is typically current-controlled, implying that a dc bias current can be adjusted to change the permeability of the core and hence the inductor's inductance. Typically, a current-controlled variable inductor is employed in this design, indicating that the permeability of the core and, consequently, the resonant tank inductor's inductance may be altered by adjusting a dc bias current (I_a). The half-bridge resonant inverter's switching power pole consists of two power diodes, denoted by D1 and D2, and two fully controlled semiconductor switches, such as MOSFETs, indicated by M1 and M2. The remaining parameters in this design are V_{dc} , C_{dc} , and C_r , which represent the inverter's dc input voltage, the capacitance of the dc blocking capacitor, and the capacitance of the resonant capacitor, respectively. In fact, this basic design, which utilizes the concept of variable inductance in lighting drivers, has been extensively employed in prior research for various purposes. For instance, a driver similar to the one illustrated in Fig. 30 was employed in [107, 109, 112] to allow universal ballasts for discharge lamps, which implies that the inverter can operate lamps with different power ratings optimally at a constant switching frequency and duty cycle. This eliminates the need for various drivers for different power rating lamps, making it a more cost-effective alternative. Furthermore, it led to the lamp's soft starting and stable, optimal performance within a designated power rating range. It should be noted that the variable inductor employed in this suggested design has a double E-core current-controlled arrangement.

Furthermore, by utilizing the same design shown in Figure 30, it is possible to minimize the striations issue in fluorescent lamps efficiently. This issue is characterized by bright and dark bands that typically appear along the lamp's tube. It usually occurs at low lamp power, typically when the lamp's power is lower than 30%, and at low temperatures, typically room temperature or lower, as in freezers, for example. Employing constant frequency and duty cycle for the inverter and only controlling the resonant inductance (L_r), the striations problem is significantly reduced. Moreover, since the control characteristic is linear, the dimming control becomes smoother. This application also utilizes a double E-core current-controlled variable inductor configuration [111].

Another realization of a variable-inductor-based electronic ballast driver is presented in [70]. The proposed configuration is based on a current-sourcing resonant inverter, and instead of controlling the switching frequency or duty cycle, the resonant inductance is being controlled similarly to the preceding applications. This design has been demonstrated to be effective in driving high-pressure discharge lamps. This design also employs a double E-core, current-controlled variable inductor [71].

In terms of light-emitting diode applications, the variable inductors concept has resolved a number of challenges in an efficient way, as reported in [113-116]. LED drivers are commonly classified into two types: passive LED drivers and switched-mode active LED drivers. The former utilizes passive components such as capacitors and inductors for performing power-factor correction (PFC), whereas the latter employs active converters for the same purpose. The main advantage of these passive LED drivers is their exceptional reliability and reduced cost because they don't have sophisticated control circuits. However, these drivers are large and heavy, with no dimming capability. Active LED drivers, on the other hand, are available in one, two, or three stages and

are typically employed in a broad range of applications owing to their small footprint and dimming capability, among several other benefits. However, the most significant drawback is that they are more expensive [148].

The line-current harmonic constraints specified by IEC 61000-3-2 Class C must be met in applications where the input power exceeds 25 W, such as but not limited to high-brightness LEDs [149]. To comply with that standard, two-stage active LED drivers are commonly employed when a universal input voltage range is adopted. Power factor correction is the first step, which uses a converter to make sure the line-current harmonic limit is fulfilled. The second stage is a dc-dc conversion stage, where dimming is possible since the output voltage delivered to LEDs could be adjusted. Since more active switches and their control circuitry are used in this design, the total cost rises. One-stage ac-dc power factor correction flyback driver with constant boost inductance is utilized, as reported in [150], to minimize the number of switches and hence the overall cost. However, employing a single-stage ac-dc PFC flyback driver with a constant boost inductance can only satisfy one of the following two constraints: 1) at high input voltage levels, the bulk capacitor should not rise to unpractical and unsafe values; and 2) at low input voltage levels, the input-current harmonics should meet the limits described by the IEC 61000-3-2 Class C standard. This difficulty can be easily handled by using variable boost inductance rather than fixed one, hence both constraints can be met. In order to guarantee that the bulk capacitor voltage is limited to safer values, the boost inductance is controlled to be constant and of a high value at high input voltage levels. It is then reduced to a lower value at low input voltage levels in order to ensure lower current harmonics, thereby satisfying the IEC 61000-3-2 Class C limits standard. A single-stage universal-input ac-dc PFC flyback driver employing a double E-core current-controlled variable inductor that is more cost-effective than two-stage solutions and able to handle both low and high input voltages efficiently and without violating line-current harmonics standards has been reported in [115, 116].

The principle of variable inductors has been also implemented to efficiently and economically equalize the branch currents in multiarray LED lamps, as reported in [113, 114]. The multiarray LED lamps typically have manufacturing imperfections that cause the current supplied to identical branches to be unequal. As a result, the brightness of each branch will differ, resulting in an overall non-uniform luminous output of the arrays that is undesirable and may have negative biological effects on human eyes. Various techniques for implementing a multiarray LED driver include variable resistance, solid-state switches, or integrated circuits in series with each branch to regulate the branch current; hence, the brightness has already been presented in previous literature. However, if there is a significant voltage drop in these regulating devices, these techniques may lead to a reduction in the efficiency of the lighting system. In order to tackle this issue, switching converters are employed in each branch instead; however, each branch requires a switching converter with active switches, which can significantly increase complexity and total cost. A solution to this problem is to use a single converter that employs a double E-core current-controlled variable inductor in series with each branch. By adjusting the branch's inductance, the multiarray LED's current in each branch can be controlled. Since this method only requires one converter, its duty cycle and frequency are fixed. In contrast to prior techniques, this approach proposes a highly reliable, economical, and efficient solution.

While it appears that employing variable inductors rather than fixed ones in lighting drivers yields several advantages, there are still certain general drawbacks that exist in all the applications discussed. These general limitations can be summarized as: 1) increased complexity in terms of control circuitry; 2) increased size due to the addition of control winding; 3) increased copper losses in the auxiliary winding of the inductor because all used inductors were current-controlled; this reduces the overall efficiency of the whole lighting system; 4) the control range is restricted to the lowest and highest inductance that the variable inductor can reach; 5) increased manufacturing cost since there are no ready-made solutions for the double E-core current-controlled variable inductor, which might increase the driver's overall cost. Considering these drawbacks, an in-depth assessment should be carried out to figure out the most effective solution.

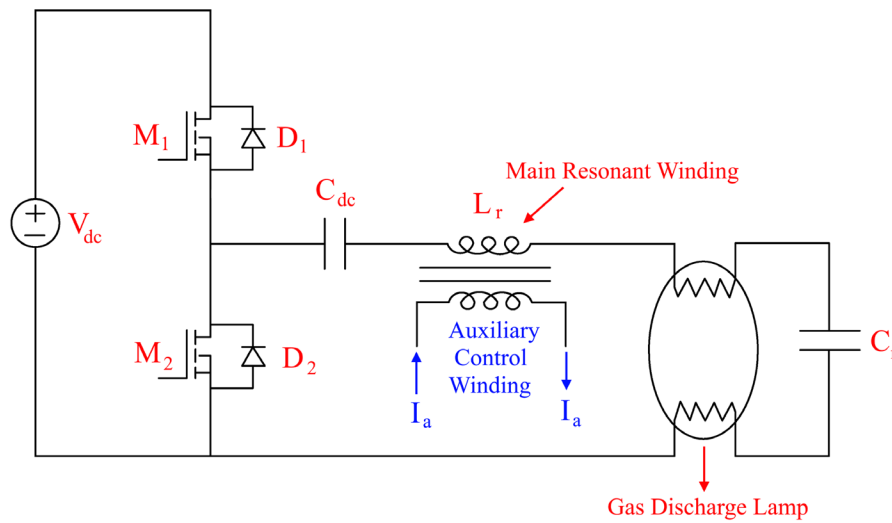


Fig. 30. The fundamental design of a magnetically-controlled electronic ballast driver.

4.1.2 Resonant Converters

Current-controlled inductors have been widely employed in a variety of resonant converter topologies to solve a range of issues [79, 80, 117-129]. For instance, operating two interleaved LLC resonant converters at the same switching frequency could result in a significant current imbalance due to mismatches between the components of the two converters. The current imbalance will result in unbalanced power distribution between the two LLC resonant converters, leading to unreliable operation. The first suggestion is to select the same capacitance and inductance values for both converters while maintaining the same switching frequency for both converters in order to achieve current balance. However, this approach is impractical and can result in increased expense and complexity since mass manufacturing of pre-selected inductances and capacitances is not feasible; instead, such components are often manufactured in standard values to allow for effective mass production. A different approach is to include an additional converter, which will operate both LLC resonant converters at the ideal switching frequency and adjust the input voltage to each LLC resonant converter, achieving current balance. Yet, this method results in a significant reduction in the overall efficiency of the two-phase interleaved LLC resonant converters due to the additional conversion stage. A novel technique has been presented in [117], whereby one LLC resonant converter is equipped with an additional fixed inductor, while the other LLC resonant converter is equipped with an additional current-controlled double E-core variable saturable inductor. By adjusting the variable inductor's inductance in one module, the component mismatch and, consequently, the current imbalance are eliminated. In this way, the switching frequency of both converters remains at the same optimal value while the resonant frequency of one LLC resonant converter is adjusted. In comparison to the prior proposed resolutions, efficiency curves suggest that this technique is more efficient. The main drawback is that designing the control circuitry of the current-controlled variable inductor to eliminate the current imbalance may increase the overall design complexity and, as a result, the overall cost.

The output voltage of dc-dc resonant converters should be regulated for different connected loads; this is usually accomplished through adjusting the switching frequency of the resonant converter's main active solid-state switches. However, the main issue is that employing switching frequency as the control parameter to regulate the output voltage would cause the electromagnetic interference filter to become larger in size and more complex to design, which would increase the resonant converter's overall size. In addition, the design of control circuits and magnetic components is quite complicated. If an alternative technique for controlling output voltage is adopted while maintaining a constant switching frequency, these issues can be overcome. The conventional approach is to add an extra conversion stage, such as a full-bridge inverter with phase-shift control, after the resonant inverter stage and before the rectification step. However, this approach increases costs owing to the increased complexity of the control circuitry and reduces efficiency due to the additional conversion stage. This issue could be solved by employing a magnetically controlled dc-dc resonant converter, as seen in Fig. 31 [118, 119, 127]. Previously, magnetic regulation of the output voltage of a dc-dc parallel resonant converter has been utilized by lighting drivers and has demonstrated several benefits over the switching frequency control technique. In the resonant tank depicted in Fig. 31, a current-controlled double-E-core variable inductor is being employed. While the switching frequency is fixed, the auxiliary winding d.c. bias current of the variable resonant inductor can be varied to regulate the converter's output voltage, represented by V_o . The converter's overall size will be reduced by using resonant inductance as the new control parameter rather than switching frequency, and designing magnetic components, driver circuitry, and electromagnetic interference filter becomes simpler, but the extra losses in the control winding will have a negative impact on the converter's overall efficiency, as reported in [119, 127], indicating that more research is required, especially with regard to this converter.

In the same manner, variable inductors have been employed in LLC resonant converters to regulate the output voltage [120-126, 128]. In fact, regulating the output voltage of LLC resonant converters by adjusting the switching frequency has the following drawbacks: complexity in designing magnetic components, electromagnetic interference filters, and driver circuitry, as well as decreased power density and increased conduction losses. All of these will cause the resonant converter's overall efficiency to drop. Yet, magnetically-regulated LLC resonant converters allowed these converters to operate at a constant switching frequency and duty cycle, overcoming these limitations. The main idea is to replace the fixed resonant inductor with a current-controlled variable inductor. Thus far, the output voltage could be adjusted while maintaining a constant switching frequency and a constant duty cycle by adjusting the resonant inductance. This idea has been utilized to build a highly efficient battery charger in which the charging process is controlled by adjusting the resonant inductance value, as described in [120]. In this proposed charger, all issues related to switching frequency control are eliminated.

Furthermore, [121, 122] has proposed another high-efficiency battery charger that utilizes variable inductors. This proposed design consists of two LLC resonant converters that share the same primary switches, with their respective outputs connected in series. In one converter, the resonant inductor is replaced by a current-controlled double E-core variable inductor, while in the other converter, it remains fixed. In order to guarantee optimal efficiency, both converters are run at a constant switching frequency close to the resonance frequency. Of the two LLC resonant converters, the one that employs a fixed resonant inductor has a fixed output voltage, while the other, which has a variable inductance, allows the battery's charging process to be controlled. Numerous benefits of this design can be summed up as follows: two LLC resonant converters paralleling allows for higher powers to be handled; smaller size of the electromagnetic interference filter, in addition to fewer complications while designing this filter; zero voltage switching for active switches and zero current switching for secondary power diodes is achievable, and consequently charging efficiency improved.

In [125], a magnetically-controlled bi-directional battery charger design comprising a full-bridge inverter and a bi-directional half-bridge LLC resonant converter has been presented. The bi-directional AC/DC conversion is carried out by the full-bridge

inverter. This full-bridge inverter functions as a power factor correction device that supplies a regulated dc voltage for the dc-dc converter in the vehicle-to-grid mode and as a full-bridge inverter that converts the dc voltage into ac in the grid-to-vehicle mode. On the other hand, the bi-directional half-bridge LLC resonant converter controls battery charging and handles the DC/DC conversion. In this bi-directional half-bridge LLC resonant converter, the fixed resonant inductor is replaced by a current-controlled variable inductor. In this approach, the resonant inductance is adjusted while the switching frequency remains constant to regulate the output DC voltage and, therefore, battery charging. In this suggested topology, using magnetic control yields a number of advantages that may be summed up as follows: higher system efficiency is possible because zero voltage and zero current switching for main and secondary switches, respectively, may be accomplished; the electromagnetic interference filter design has been optimized and simplified, which will substantially reduce the charger's overall size.

A low-power magnetically regulated single-stage AC/DC LLC resonant converter has been presented in [126]. The suggested topology comprises a boost power factor correction converter and a half-bridge LLC resonant converter, both of which share the same primary active switches. The boost converter performs a power factor correction function and regulates the input voltage to the resonant converter, while the latter regulates the output DC voltage. Instead of employing the switching frequency control technique, a current-controlled variable inductor replaced the fixed resonant inductor in the LLC resonant converter. As a result, by modifying the resonant inductance value, the LLC resonant converter's output voltage can be regulated. Numerous benefits are seen, all of which are similar to previously stated applications; the constant switching frequency operation simplifies the design of magnetic components and control circuitry. In addition, the operation at this constant frequency allowed the operation to approach the resonant frequency, thereby guaranteeing optimal operation and better efficiency. Furthermore, soft switching for all solid-state switches, whether primary or secondary, is achieved, which increases system efficiency.

Variable inductors have also been employed to address the cross-regulation issue in the multiple output LLC resonant converter, as presented in [128]. The proposed topology consists of an asymmetric half-bridge inverter, followed by a double E-core current-controlled variable resonant inductor for each output channel. Each channel's output voltage is regulated independently by adjusting the channel's resonant inductance. Variations in the input voltage and/or output power typically result in fluctuations in the converter's output voltage. If the technique of switching frequency control is utilized instead of the magnetic control technique, a broad switching frequency range is employed to account for both variations and achieve the necessary output voltage regulation. Within the suggested topology, the output voltage is controlled by the magnetic control technique in the event of fluctuations in output power, but on the other hand, the output voltage is still being regulated by the switching frequency control technique when the input voltage varies. Employing magnetic control has in fact significantly reduced the switching frequency control range, and consequently the following benefits have been reported: the cross-regulation issue is resolved and each channel output voltage can be controlled independently; the design of magnetic components, electromagnetic interference filter, and control circuitry is further simplified and optimized; soft switching is possible for all primary and secondary solid-state switches; and an unlimited number of channels can be added to the proposed topology.

Although using magnetic control in resonant converters has several advantages, as discussed in the earlier applications, there are a few common drawbacks as well. In short, these common shortcomings may be summarized as follows: increasing losses in the control winding of the variable inductor will deteriorate the converter's overall efficiency, and the voltage regulation range is usually limited due to the limited resonant inductance range. Though it appears that the advantages exceed these drawbacks, additional research is needed to address these issues or determine the best design compromise.

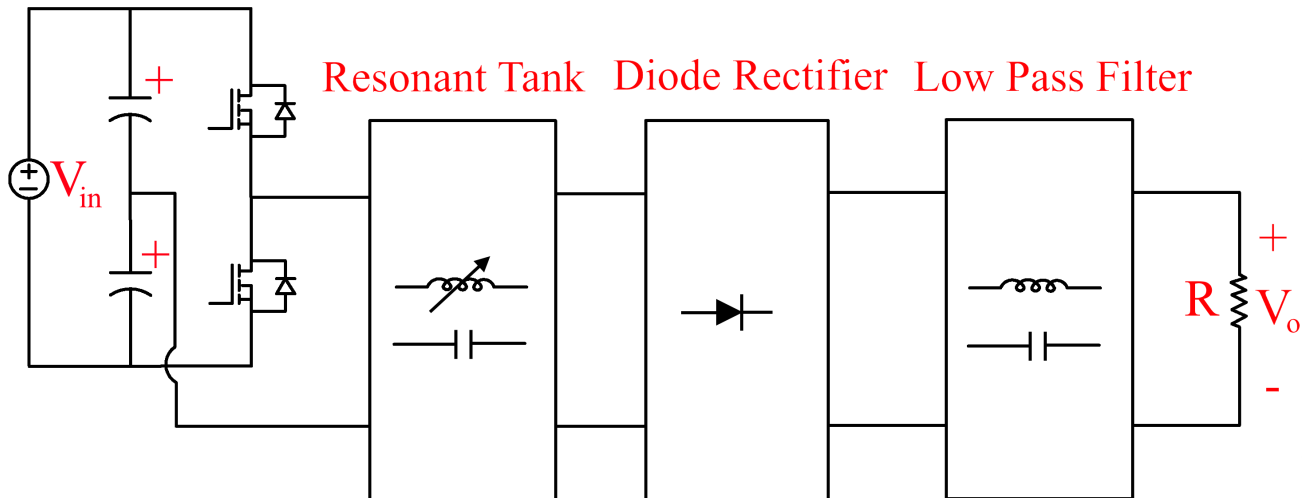


Fig. 31. The basic design of a magnetically-controlled dc-dc resonant converter.

4.1.3 Dual Active Bridge Converters

Dual active bridge (DAB) converters are one of the most common solid-state transformers used in a variety of applications to bidirectionally regulate power flow between two sources. In DAB converters, phase shift control between the two full bridges of the converter is the conventional power flow control approach. However, in fact, the phase shift modulation control technique achieves high efficiencies only when voltage levels match the transformer's turns ratio. A voltage mismatch will lead to an increase in the RMS current, thereby increasing the inductor's and transformer's copper losses as well as the conduction losses of solid-state switches. Furthermore, a circulating current will be generated from the phase shift between the voltage and current applied to the transformer, which will further reduce the efficiency. Additionally, with light loads, zero-voltage switching is not feasible, which would subsequently deteriorate the efficiency under these conditions. In reality, a number of controlling strategies have been proposed to regulate the power flow between the two dc sources. One such strategy involves using frequency control rather than phase shift, but it has increased the complexity of control circuits and is further limited by the magnetic components [72, 145]. Variable inductors were used to get around these difficulties, as reported in [72, 130, 131]. To address these challenges, the suggested design used both the phase shift control approach and the inductance control technique. The proposed topology is depicted in Fig. 32, which represents a bidirectional isolated dc-dc converter. It is primarily composed of two full bridge inverters, the primary and secondary, coupled via a high-frequency transformer and a power transfer inductor. The power transferred in this proposed topology depends on the following: the phase shift between the primary and secondary full bridge inverters; the input and output voltages, represented as V_{in} and V_o ; the transformer turns ratio, expressed as N_p/N_s ; and the variable inductor's reactance, which in turn depends on the switching frequency and the variable inductor's inductance. This suggests that by adjusting the variable inductance as the new control parameter, the power transfer between the two sources could be achieved. The variable inductor employed is a double E-core current-controlled type. The following is a summary of the benefits of this proposed topology: 1) the zero-voltage switching range was extended by increasing the inductance at light loading conditions, which resulted in improving the efficiency due to the soft switching improvement; on the other hand, the inductance was decreased at heavy loading conditions in order to reduce the circulating current and hence improve the efficiency; and the overall result is an increase in the converter's efficiency over a wide range of loads; 2) the power transfer characteristics were linearized, which can help in simplifying the design of the converter's control system; 3) improvement in the transient response as the added control parameter, the variable inductance, can aid in stabilizing the system's dynamic response upon any disturbance. On the other hand, two limits were observed: the zero-voltage switching range was limited and not extended significantly by the variable inductance, and optimization in terms of the converter's size was not feasible. In order to overcome these two difficulties, further study is still required.

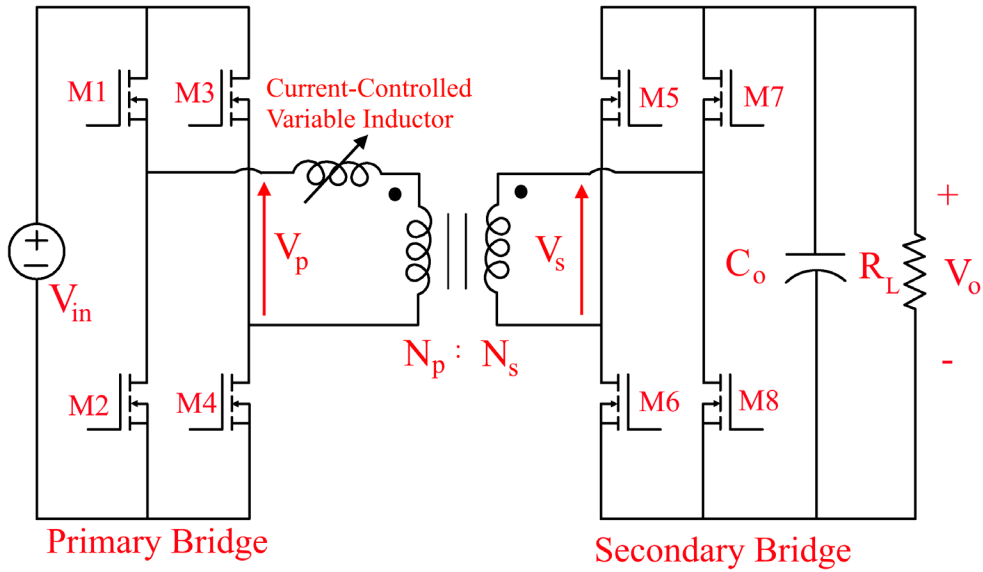


Fig. 32. The basic design of magnetically-controlled dual-active-bridge converter.

4.2 Future Research

It has become evident that tunable magnetics for power electronics, particularly current-controlled types, are promising for numerous applications, as detailed previously. In contrast, voltage-controlled tunable magnetics provide a more advantageous option than current-controlled ones; however, the high cost of this technology has prevented its application in the power electronics domain. Yet, despite all of the advantages that variable inductors have achieved in various power electronic applications, off-the-shelf solutions are still not available.

Therefore, in order to meet the industrial application needs, further research is crucial. Further research on current-controlled variable inductors needs to focus on the following points: first, as previously mentioned, the typical variation of inductance with

the DC control current was non-linear; therefore, different magnetic materials may be utilized to achieve more linear inductance-current characteristics; in fact, the non-linearity of the inductance-current relationship does not allow smooth and precise control; and second, different structures and configurations of the magnetic core should be investigated in order to optimize the inductor's overall size, extend the variable inductance tunability range, and minimize iron losses. It is essential to note that since cost is a dominant factor, any further research addressing these two points should take into consideration the inductor's overall cost.

For voltage-controlled variable inductors, the following points need to be addressed: first, in order to reduce the cost of this type, extensive research regarding the cost of the piezoelectric and ferromagnetic layers must be carried out, considering new manufacturing processes and other advancements in material science; second, new structures, configurations, and materials should be investigated in order to achieve a higher inductance tunability range at a lower control voltage, taking into consideration that the variation of inductance with the applied control voltage should be linear in order to achieve smooth control.

5. CONCLUSIONS

In this article, a comprehensive review of the tunable magnetics concept for power electronic applications has been presented. The principle of operation, various configurations and applications, and merits and drawbacks of various current-controlled and voltage-controlled variable inductors have been thoroughly examined. The primary objective of this review is to provide full guidance on the significance of the concept of tunable magnetics in power electronics and future research guidelines in this field. In summary, the main conclusion of this article is that current-controlled variable inductors, particularly the double E-core configuration, are currently widely employed in a variety of power electronic applications. This type was utilized primarily to efficiently regulate output voltage and power in lighting drivers, give additional control freedom in resonant converters, and improve the efficiency of dual active bridge converters, among other uses. However, in some of these applications, the unoptimized size, the inductance non-linear control characteristic, and higher losses in control winding still present a significant challenge. Furthermore, it was shown that, despite the fact that voltage-controlled variable inductors are superior to current-controlled ones owing to their broader inductance tunability range, smaller size, and increased efficiency, their primary reason that limits their applications in power electronic applications is their expensive cost.

REFERENCES

- [1] L. Umanand, "Design of Magnetics," in *Power Electronics: Essentials and Applications*, 1 ed. New Delhi, India: Wiley India Pvt. Ltd., 2009, pp. 369-416.
- [2] W. G. Hurley and W. H. Wölflé, "Inductance," in *Transformers and Inductors for Power Electronics: Theory, Design and Applications*, 1 ed. United Kingdom: John Wiley & Sons Ltd, 2013, pp. 25-54.
- [3] N. Soltau, D. Eggers, K. Hameyer, and R. W. D. Doncker, "Iron Losses in a Medium-Frequency Transformer Operated in a High-Power DC–DC Converter," *IEEE Transactions on Magnetics*, vol. 50, no. 2, pp. 953-956, 2014, doi: 10.1109/TMAG.2013.2283733.
- [4] K. Górecki and K. Detka, "Analysis of influence of losses in the core of the inductor on parameters of the buck converter," in *2018 Baltic URSI Symposium (URSI)*, 15-17 May 2018 2018, pp. 129-132, doi: 10.23919/URSI.2018.8406725.
- [5] Z. Yan, Z. Weibo, and T. Guanghui, "A Core Loss Calculation Method for DC/DC Power Converters Based on Sinusoidal Losses," *IEEE Transactions on Power Electronics*, vol. 38, no. 1, pp. 692-702, 2023, doi: 10.1109/TPEL.2022.3199041.
- [6] A. Dhole, S. K. Roy, and K. Basu, "Estimation and Measurement of Power Loss in a High Frequency Inductor for a DAB based DC-DC Converter," in *2021 National Power Electronics Conference (NPEC)*, 15-17 Dec. 2021 2021, pp. 1-6, doi: 10.1109/NPEC52100.2021.9672537.
- [7] S. Miao, W. Liu, and J. Gao, "Single-Inductor Boost Converter With Ultrahigh Step-Up Gain, Lower Switches Voltage Stress, Continuous Input Current, and Common Grounded Structure," *IEEE Transactions on Power Electronics*, vol. 36, no. 7, pp. 7841-7852, 2021, doi: 10.1109/TPEL.2020.3047660.
- [8] H. Y. Chung, F. N. K. Poon, C. P. Liu, and M. H. Pong, "Analysis of buck-boost converter inductor loss using a simple online B-H curve tracer," in *APEC 2000. Fifteenth Annual IEEE Applied Power Electronics Conference and Exposition (Cat. No.00CH37058)*, 6-10 Feb. 2000 2000, vol. 2, pp. 640-646 vol.2, doi: 10.1109/APEC.2000.822572.
- [9] R. Guan *et al.*, "A Medium Voltage Input Multiport Isolated Output DC Transformer With Power Self-Balancing and Output Fault Isolation," *IEEE Transactions on Power Electronics*, vol. 38, no. 4, pp. 4771-4786, 2023, doi: 10.1109/TPEL.2022.3230850.
- [10] R. Kasashima, S. Nakagawa, K. Nishimoto, Y. Kado, and K. Wada, "Power loss analysis of 10kW three-way isolated DC/DC converter using SiC-MOSFETs as a power routing unit for constructing 400V DC microgrid systems," in *IECON 2016 - 42nd Annual Conference of the IEEE Industrial Electronics Society*, 23-26 Oct. 2016 2016, pp. 1394-1399, doi: 10.1109/IECON.2016.7793215.
- [11] C. Samende, N. Mugwisi, D. J. Rogers, E. Chatzinikolaou, F. Gao, and M. McCulloch, "Power Loss Analysis of a Multiport DC – DC Converter for DC Grid Applications," in *IECON 2018 - 44th Annual Conference of the IEEE Industrial Electronics Society*, 21-23 Oct. 2018 2018, pp. 1412-1417, doi: 10.1109/IECON.2018.8591730.
- [12] L. Jia, S. Lakshminathan, X. Li, and Y. F. Liu, "New Modeling Method and Design Optimization for a Soft-Switched DC–DC Converter," *IEEE Transactions on Power Electronics*, vol. 33, no. 7, pp. 5754-5772, 2018, doi: 10.1109/TPEL.2017.2751064.
- [13] I. Talebian, P. Alavi, V. Marzang, E. Babaei, and A. Khoshkbar-Sadigh, "Analysis, Design, and Investigation of a Soft-Switched Buck Converter With High Efficiency," *IEEE Transactions on Power Electronics*, vol. 37, no. 6, pp. 6899-6912, 2022, doi: 10.1109/TPEL.2021.3132463.
- [14] H. Akagi, T. Yamagishi, N. M. L. Tan, S. i. Kinouchi, Y. Miyazaki, and M. Koyama, "Power-Loss Breakdown of a 750-V 100-kW 20-kHz Bidirectional Isolated DC–DC Converter Using SiC-MOSFET/SBD Dual Modules," *IEEE Transactions on Industry Applications*, vol. 51, no. 1, pp. 420-428, 2015, doi: 10.1109/TIA.2014.2331426.
- [15] Z. Dang and J. A. A. Qahouq, "Evaluation of High-Current Toroid Power Inductor With NdFeB Magnet for DC–DC Power Converters," *IEEE Transactions on Industrial Electronics*, vol. 62, no. 11, pp. 6868-6876, 2015, doi: 10.1109/TIE.2015.2436361.
- [16] M. Beraki, J. P. Trovão, and M. Perdigão, "Design of Variable Inductor for Powertrain DC-DC Converter," in *2019 IEEE 28th International Symposium on Industrial Electronics (ISIE)*, 12-14 June 2019 2019, pp. 822-827, doi: 10.1109/ISIE.2019.8781250.
- [17] M. Liserre *et al.*, "Voltage Controlled Magnetic Components for Power Electronics," *IEEE Power Electronics Magazine*, vol. 10, no. 2, pp. 40-48, 2023, doi: 10.1109/MPEL.2023.3273892.
- [18] F. Reverter and M. Gasulla, "Optimal Inductor Current in Boost DC/DC Converters Operating in Burst Mode Under Light-Load Conditions," *IEEE Transactions on Power Electronics*, vol. 31, no. 1, pp. 15-20, 2016, doi: 10.1109/TPEL.2015.2454331.
- [19] F. Reverter and M. Gasulla, "Optimal Inductor Current in Boost DC/DC Converters Regulating the Input Voltage Applied to Low-Power Photovoltaic Modules," *IEEE Transactions on Power Electronics*, vol. 32, no. 8, pp. 6188-6196, 2017, doi: 10.1109/TPEL.2016.2619482.

- [20] M. Beraki, M. Perdigao, F. Machado, and J. P. Trovão, "Auxiliary converter for variable inductor control in a DC-DC converter application," in *2016 51st International Universities Power Engineering Conference (UPEC)*, 6-9 Sept. 2016 2016, pp. 1-6, doi: 10.1109/UPEC.2016.8114107.
- [21] M. Beraki, J. P. Trovão, M. Perdigao, and F. Machado, "Bidirectional DC-DC Converter Using Variable Inductor Concept for Electric Vehicle Applications," in *2016 IEEE Vehicle Power and Propulsion Conference (VPPC)*, 17-20 Oct. 2016 2016, pp. 1-6, doi: 10.1109/VPPC.2016.7791626.
- [22] M. W. Beraki, J. P. F. Trovão, M. S. Perdigão, and M. R. Dubois, "Variable Inductor Based Bidirectional DC-DC Converter for Electric Vehicles," *IEEE Transactions on Vehicular Technology*, vol. 66, no. 10, pp. 8764-8772, 2017, doi: 10.1109/TVT.2017.2710262.
- [23] A. V. d. Bossche and V. C. Valchev, "Fundamentals of Magnetic Theory," in *Inductors and Transformers for Power Electronics*. United States of America: CRC Press, 2005, pp. 26-54.
- [24] B. D. Cullity and C. D. Graham, "Definitions and Units," in *Introduction to Magnetic Materials*, 2 ed. New Jersey, USA: John Wiley & Sons, 2009, pp. 1-20.
- [25] Magnetics. "Curve Fit Equation Tool." Magnetics, Inc. <https://www.mag-inc.com/Design/Design-Tools/Curve-Fit-Equation-Tool> (accessed September 28, 2023).
- [26] J. Gareau, A. Emadi, and B. Bilgin, "Power Inductor Optimization Using Non-linear Magnetization Characteristics," in *2020 IEEE Transportation Electrification Conference & Expo (ITEC)*, 23-26 June 2020 2020, pp. 992-999, doi: 10.1109/ITEC48692.2020.9161550.
- [27] S. Choi, J. Imaoka, and M. Yamamoto, "Modeling and Design Method of Coupled Inductor Using Powder Core with Concentrated Air Gap," in *2022 IEEE Energy Conversion Congress and Exposition (ECCE)*, 9-13 Oct. 2022 2022, pp. 1-5, doi: 10.1109/ECCE50734.2022.9947578.
- [28] Magnetics. "Powder Core Documents." Magnetics, Inc. <https://www.mag-inc.com/Design/Technical-Documents/Powder-Core-Documents> (accessed September 29, 2023).
- [29] T. Aoki, J. Imaoka, M. Yamamoto, and K. Yoshimoto, "Improving DC superimposition characteristics of powder cores by applying coupled inductors in multi-phase boost converter," *IET Power Electronics*, vol. 15, no. 3, pp. 237-250, 2022, doi: <https://doi.org/10.1049/pel.2.12226>.
- [30] R. Jez, "Influence of the Distributed Air Gap on the Parameters of an Industrial Inductor," *IEEE Transactions on Magnetics*, vol. 53, no. 11, pp. 1-5, 2017, doi: 10.1109/TMAG.2017.2699120.
- [31] C. Guozhu, K. M. Smedley, and Q. Zhaoming, "Tuned power inductors for hybrid active power filter with structure of hybrid magnetic core, distributed air gaps and three-phase five column," in *IECON'03. 29th Annual Conference of the IEEE Industrial Electronics Society (IEEE Cat. No.03CH37468)*, 2-6 Nov. 2003 2003, vol. 3, pp. 2023-2028 Vol.3, doi: 10.1109/IECON.2003.1280554.
- [32] D. K. Saini, A. Ayachit, A. Reatti, and M. K. Kazimierczuk, "Analysis and Design of Choke Inductors for Switched-Mode Power Inverters," *IEEE Transactions on Industrial Electronics*, vol. 65, no. 3, pp. 2234-2244, 2018, doi: 10.1109/TIE.2017.2740847.
- [33] F. Banitorfian, F. Eshghabadi, A. A. Manaf, N. M. Noh, and M. T. Mustaffa, "Radio-frequency silicon-based CMOS-compatible MEMS variable solenoid micro-fluidic inductor with Galinstan-based continuously-adjustable turn-ratio technique," in *2015 6th Asia Symposium on Quality Electronic Design (ASQED)*, 4-5 Aug. 2015 2015, pp. 90-93, doi: 10.1109/ACQED.2015.7274014.
- [34] N. D. Benavides and P. L. Chapman, "Boost Converter with a Reconfigurable Inductor," in *2007 IEEE Power Electronics Specialists Conference*, 17-21 June 2007 2007, pp. 1695-1700, doi: 10.1109/PESC.2007.4342253.
- [35] S. Aliouane, A. B. Kouki, and R. Aigner, "RF-MEMS switchable inductors for tunable bandwidth BAW filters," in *5th International Conference on Design & Technology of Integrated Systems in Nanoscale Era*, 23-25 March 2010 2010, pp. 1-6, doi: 10.1109/DTIS.2010.5487536.
- [36] A. Nieuwoudt and Y. Massoud, "Design optimization of switchable multi-port spiral inductors," *Analog Integrated Circuits and Signal Processing*, vol. 51, no. 3, pp. 195-200, 2007/06/01 2007, doi: 10.1007/s10470-007-9068-2.
- [37] R. R. Mansour, M. Bakri-Kassem, M. Daneshmand, and N. Messiha, "RF MEMS devices," in *Proceedings International Conference on MEMS, NANO and Smart Systems*, 23-23 July 2003 2003, pp. 103-107, doi: 10.1109/ICMENS.2003.1221974.
- [38] S. S. Saberhosseini, B. A. Ganji, A. Razeghi, and Z. Mahmoudi, "Modeling & simulation of MEMS spiral inductor," in *2016 24th Iranian Conference on Electrical Engineering (ICEE)*, 10-12 May 2016 2016, pp. 507-510, doi: 10.1109/IranianCEE.2016.7585574.
- [39] C. D. Patel and G. M. Rebeiz, "An RF-MEMS switch for high-power applications," in *2012 IEEE/MTT-S International Microwave Symposium Digest*, 17-22 June 2012 2012, pp. 1-3, doi: 10.1109/MWSYM.2012.6259363.
- [40] I. Gmati, H. Boussetta, M. A. Kallala, and K. Besbes, "Wide-range RF MEMS variable inductor using micro pump actuator," in *2008 2nd International Conference on Signals, Circuits and Systems*, 7-9 Nov. 2008 2008, pp. 1-4, doi: 10.1109/ICSCS.2008.4746937.
- [41] P. Piljae, K. Cheon Soo, P. Mun Yang, K. Sung Do, and Y. Hyun Kyu, "Variable inductance multilayer inductor with MOSFET switch control," *IEEE Electron Device Letters*, vol. 25, no. 3, pp. 144-146, 2004, doi: 10.1109/LED.2003.822670.
- [42] I. El Gmati et al., "Liquid RF MEMS variable inductor," *Procedia Engineering*, vol. 5, pp. 1380-1383, 2010/01/01/ 2010, doi: <https://doi.org/10.1016/j.proeng.2010.09.372>.
- [43] T. A. Smith and S. Dimitrijev, "Using the on-resistance of a power MOSFET to control a DC-DC converter," in *IEEE APCCAS 1998. 1998 IEEE Asia-Pacific Conference on Circuits and Systems. Microelectronics and Integrating Systems. Proceedings (Cat. No.98EX242)*, 24-27 Nov. 1998 1998, pp. 731-733, doi: 10.1109/APCCAS.1998.743925.
- [44] W. Wolfle, W. G. Hurley, and S. Lambert, "Quasi-active power factor correction: the role of variable inductance," in *2001 IEEE 32nd Annual Power Electronics Specialists Conference (IEEE Cat. No.01CH37230)*, 17-21 June 2001 2001, vol. 4, pp. 2078-2083 vol. 4, doi: 10.1109/PESC.2001.954427.
- [45] E. Stenglein and M. Albach, "Analytical calculation method for the non-linear characteristic of ferrite-cored inductors with stepped air gap," *Electrical Engineering*, vol. 99, no. 1, pp. 421-429, 2017/03/01 2017, doi: 10.1007/s00202-016-0432-z.
- [46] Z. Yang, H. Suryanarayana, and F. Wang, "An Improved Design Method for Gapped Inductors Considering Fringing Effect," in *2019 IEEE Applied Power Electronics Conference and Exposition (APEC)*, 17-21 March 2019 2019, pp. 1250-1256, doi: 10.1109/APEC.2019.8721811.
- [47] S. Choi, J. Imaoka, and M. Yamamoto, "Design of Coupled Inductor Using Powder Core with Concentrated Air Gap in Multiphase Operation," *IEEE Transactions on Industry Applications*, pp. 1-10, 2023, doi: 10.1109/TIA.2023.3344558.
- [48] L. Solimene, D. Cittanti, F. Mandrile, S. Musumeci, and R. Bojoi, "Optimal Air Gap Length Design in Powder Core Inductors," *IEEE Transactions on Magnetics*, vol. 59, no. 11, pp. 1-5, 2023, doi: 10.1109/TMAG.2023.3289391.
- [49] J. D. Pollock, W. Lundquist, and C. R. Sullivan, "Predicting inductance roll-off with dc excitations," in *2011 IEEE Energy Conversion Congress and Exposition*, 17-22 Sept. 2011 2011, pp. 2139-2145, doi: 10.1109/ECCE.2011.6064051.
- [50] F. Battal, S. Balci, and S. İ., "An Analysis of High Power Inductor Vibration Behavior in Terms of Air Gaps," in *2019 International Conference on Power Generation Systems and Renewable Energy Technologies (PGSRET)*, 26-27 Aug. 2019 2019, pp. 1-6, doi: 10.1109/PGSRET.2019.8882655.
- [51] N. Toprak, K. Dawood, and G. Kömürgöz, "Optimization of the number of the airgaps in the shunt reactor using finite element method," in *2022 5th International Conference on Power Electronics and their Applications (ICPEA)*, 29-31 March 2022 2022, vol. 1, pp. 1-5, doi: 10.1109/ICPEA51060.2022.9791139.
- [52] A. Walker, G. Vakil, and C. Gerada, "Novel Core Designs to Miniaturise Passive Magnetic Components," in *2018 IEEE Transportation Electrification Conference and Expo (ITEC)*, 13-15 June 2018 2018, pp. 644-649, doi: 10.1109/ITEC.2018.8449959.
- [53] S. Brandt, M. Meissner, N. Polap, G. Schierle, and K. F. Hoffmann, "A Survey on Adjustable Inductances for Power Electronic Circuits," in *PCIM Europe 2022; International Exhibition and Conference for Power Electronics, Intelligent Motion, Renewable Energy and Energy Management*, 10-12 May 2022 2022, pp. 1-9, doi: 10.30420/565822219.
- [54] D. Thenathayalan and J. H. Park, "Highly Flexible High-Efficiency Multiple-Resonant Wireless Power Transfer System Using a Controllable Inductor," *IEEE Journal of Emerging and Selected Topics in Power Electronics*, vol. 7, no. 3, pp. 1914-1930, 2019, doi: 10.1109/JESTPE.2018.2867637.

- [55] M. M. Teymoori and J. Merrikhi Ahangarkolaei, "A core-displacement method tunable inductor using micro-electro-mechanical-systems technology," *Indian J. Sci. Technol.*, vol. 8, no. 11, 2015/6/8 2015, doi: 10.17485/ijst/2015/v8i11/71770.
- [56] G. Schierle, M. Meissner, H. Saß, and K. F. Hoffmann, "Analysis of Material Mixtures for the Characteristics of a Field Coupled Current Controlled Adjustable Inductance," in *2023 25th European Conference on Power Electronics and Applications (EPE'23 ECCE Europe)*, 4-8 Sept. 2023 2023, pp. 1-10, doi: 10.23919/EPE23ECCEEurope58414.2023.10264336.
- [57] G. Schierle, M. Meissner, and K. F. Hoffmann, "Analysis and Discussion of a Concept for an Adjustable Inductance Based on an Impact of an Orthogonal Magnetic Field," in *2022 24th European Conference on Power Electronics and Applications (EPE'22 ECCE Europe)*, 5-9 Sept. 2022 2022, pp. 1-10.
- [58] J. Yuan, X. Zheng, and F. Chen, "Analysis and Optimized Design of a Novel Compact Orthogonal Controllable Reactor," *IEEE Transactions on Power Delivery*, vol. 37, no. 6, pp. 4527-4538, 2022, doi: 10.1109/TPWRD.2022.3150303.
- [59] S. Zurek, J. Hall, T. Kutrowski, and A. Cheer, "Experimental Verification of 2.4 kVAr and 12 kVAr Prototype Variable Inductors Controlled By Virtual Air Gaps With Magnetic Orthogonality," *IEEE Transactions on Power Delivery*, vol. 37, no. 6, pp. 4880-4887, 2022, doi: 10.1109/TPWRD.2022.3162174.
- [60] G. Schierle, M. Meissner, and K. F. Hoffmann, "Non-linear effects of operation temperature on a field-coupled current-controlled inductance," *Archives of Electrical Engineering*, vol. 72, no. No 2, pp. 541-553, 2023.06.19 2023, doi: 10.24425/eee.2023.145424.
- [61] G. Schierle, M. Meissner, H. Sass, and K. F. Hoffmann, "Experimental Analysis of the Temperature Dependency of an Orthogonal Field-Coupled Current Controlled Adjustable Inductance," in *PCIM Europe 2023; International Exhibition and Conference for Power Electronics, Intelligent Motion, Renewable Energy and Energy Management*, 9-11 May 2023 2023, pp. 1-10, doi: 10.30420/566091184.
- [62] Z. Wang *et al.*, "Development of a New Type of HTS Controllable Reactor With Orthogonally Configured Core," *IEEE Transactions on Applied Superconductivity*, vol. 27, no. 4, pp. 1-5, 2017, doi: 10.1109/TASC.2017.2653205.
- [63] H. Wouters, C. Suarez, and W. Martinez, "Orthogonal Biasing Controllable Inductor using a Commercial Hollow Toroid Core," in *2023 11th International Conference on Power Electronics and ECCE Asia (ICPE 2023 - ECCE Asia)*, 22-25 May 2023 2023, pp. 294-300, doi: 10.23919/ICPE2023-ECCEAsia54778.2023.10213978.
- [64] P. Zacharias, T. Kleeb, F. Fenske, J. Wende, and J. Pfeiffer, "Controlled magnetic devices in power electronic applications," in *2017 19th European Conference on Power Electronics and Applications (EPE'17 ECCE Europe)*, 11-14 Sept. 2017 2017, pp. P.1-P.10, doi: 10.23919/EPE17ECCEurope.2017.8099004.
- [65] Z. Wang *et al.*, "Performance Analysis and Prototype Design of a D-Core-Type Single-Phase HTS Controllable Reactor," *IEEE Transactions on Applied Superconductivity*, vol. 26, no. 4, pp. 1-4, 2016, doi: 10.1109/TASC.2016.2539151.
- [66] Y. Zhang *et al.*, "Study on AC Loss Characteristics in HTS Windings of a HTS Controllable Reactor With Orthogonally Configured Core," *IEEE Transactions on Applied Superconductivity*, vol. 29, no. 5, pp. 1-5, 2019, doi: 10.1109/TASC.2019.2898695.
- [67] D. S. L. Dolan and P. W. Lehn, "Analysis of a Virtual Air Gap Variable Reactor," in *2007 IEEE Power Electronics Specialists Conference*, 17-21 June 2007 2007, pp. 1182-1187, doi: 10.1109/PESC.2007.4342160.
- [68] J. Pfeiffer, P. Küster, I. E. M. Schulz, J. Friebe, and P. Zacharias, "Review of Flux Interaction of Differently Aligned Magnetic Fields in Inductors and Transformers," *IEEE Access*, vol. 9, pp. 2357-2381, 2021, doi: 10.1109/ACCESS.2020.3047156.
- [69] A. Konrad and J. F. Brudny, "An improved method for virtual air gap length computation," *IEEE Transactions on Magnetics*, vol. 41, no. 10, pp. 4051-4053, 2005, doi: 10.1109/TMAG.2005.854987.
- [70] M. Gulko, D. Medini, and S. Ben-Yaakov, "Inductor-controlled current-sourcing resonant inverter and its application as a high pressure discharge lamp driver," in *Proceedings of 1994 IEEE Applied Power Electronics Conference and Exposition - ASPEC'94*, 13-17 Feb. 1994 1994, pp. 434-440 vol.1, doi: 10.1109/APEC.1994.316366.
- [71] D. Medini and S. Ben-Yaakov, "A current-controlled variable-inductor for high frequency resonant power circuits," in *Proceedings of 1994 IEEE Applied Power Electronics Conference and Exposition - ASPEC'94*, 13-17 Feb. 1994 1994, pp. 219-225 vol.1, doi: 10.1109/APEC.1994.316396.
- [72] S. Saeed, J. Garcia, and R. Georgiou, "Dual-Active-Bridge Isolated DC-DC Converter With Variable Inductor for Wide Load Range Operation," *IEEE Transactions on Power Electronics*, vol. 36, no. 7, pp. 8028-8043, 2021, doi: 10.1109/TPEL.2020.3048928.
- [73] A. P. Mendes, B. Baptista, M. S. Perdigão, and A. M. S. Mendes, "Experimental analysis of a DC current-controlled variable inductor in a DC-DC converter," in *2019 IEEE International Conference on Industrial Technology (ICIT)*, 13-15 Feb. 2019 2019, pp. 440-445, doi: 10.1109/ICIT.2019.8755161.
- [74] M. Beraki, J. P. Trovão, and M. Perdigão, "Characterization of variable inductors using finite element analysis," *Simulation Modelling Practice and Theory*, vol. 97, p. 101952, 2019/12/01/ 2019, doi: <https://doi.org/10.1016/j.simpat.2019.101952>.
- [75] H. Liu, L. Qu, Q. Tong, and G. Jia, "Novel filter approach for ripple-free input current boost converters based on variable inductors," *Journal of Power Electronics*, vol. 23, no. 7, pp. 1073-1085, 2023/07/01 2023, doi: 10.1007/s43236-023-00610-6.
- [76] L. Solimene, F. Corti, S. Musumeci, C. S. Ragusa, A. Reatti, and E. Cardelli, "Design and modelling of a controlled saturable inductor for an LCC-S compensated WPT system," *Journal of Magnetism and Magnetic Materials*, vol. 564, p. 170056, 2022/12/15/ 2022, doi: <https://doi.org/10.1016/j.jmmm.2022.170056>.
- [77] M. S. Perdigão, S. F. Ferreira, M. Martins, A. S. Mendes, and J. M. Alonso, "Finite element analysis of a variable inductor for an RSCC based LED lamp driver," in *2015 IEEE Industry Applications Society Annual Meeting*, 18-22 Oct. 2015 2015, pp. 1-8, doi: 10.1109/IAS.2015.7356874.
- [78] Z. Zhang *et al.*, "All-Fixed Switching Frequency Control of CRM Boost PFC Converter Based on Variable Inductor in a Wide Input Voltage Range," in *2019 IEEE Energy Conversion Congress and Exposition (ECCE)*, 29 Sept.-3 Oct. 2019 2019, pp. 1434-1441, doi: 10.1109/ECCE.2019.8913202.
- [79] T. Pereira, Y. Wei, Y. Pascal, H. A. Mantooth, and M. Liserre, "Self-Tuning Multiport Resonant DC/DC Converter Based on Actively-Controlled Inductors for Hybrid Storage System Integration," *IEEE Transactions on Power Electronics*, vol. 38, no. 4, pp. 4787-4804, 2023, doi: 10.1109/TPEL.2022.3232188.
- [80] T. Pereira, Y. Pascal, M. Liserre, Y. Wei, and H. A. Mantooth, "Multiport Resonant DC-DC Converter using Actively-Controlled Inductors for Hybrid Energy Storage System Integration," in *2022 IEEE Applied Power Electronics Conference and Exposition (APEC)*, 20-24 March 2022 2022, pp. 1154-1161, doi: 10.1109/APEC43599.2022.9773497.
- [81] Y. Wei, Q. Luo, and A. Mantooth, "Overview of Modulation Strategies for LLC Resonant Converter," *IEEE Transactions on Power Electronics*, vol. 35, no. 10, pp. 10423-10443, 2020, doi: 10.1109/TPEL.2020.2975392.
- [82] M. S. Perdigão, M. F. Menke, Á. R. Seidel, R. A. Pinto, and J. M. Alonso, "A Review on Variable Inductors and Variable Transformers: Applications to Lighting Drivers," *IEEE Transactions on Industry Applications*, vol. 52, no. 1, pp. 531-547, 2016, doi: 10.1109/TIA.2015.2483580.
- [83] S. Saeed, J. Garcia, M. S. Perdigão, V. S. Costa, B. Baptista, and A. M. S. Mendes, "Improved inductance calculation in variable power inductors by adjustment of the reluctance model through magnetic path analysis," in *2019 IEEE Energy Conversion Congress and Exposition (ECCE)*, 29 Sept.-3 Oct. 2019 2019, pp. 6634-6640, doi: 10.1109/ECCE.2019.8913160.
- [84] F. Banitorfian *et al.*, "A novel tunable water-based RF MEMS solenoid inductor," in *RSM 2013 IEEE Regional Symposium on Micro and Nanoelectronics*, 25-27 Sept. 2013 2013, pp. 58-61, doi: 10.1109/RSM.2013.6706472.
- [85] J. Lou, D. Reed, M. Liu, and N. X. Sun, "Electrostatically tunable magnetoelectric inductors with large inductance tunability," *Appl. Phys. Lett.*, vol. 94, no. 11, p. 112508, 2009/3/16 2009, doi: 10.1063/1.3103273.

- [86] Y. Yan *et al.*, "Correlation between tunability and anisotropy in magnetoelectric voltage tunable inductor (VTI)," *Scientific Reports*, vol. 7, no. 1, p. 16008, 2017/11/22 2017, doi: 10.1038/s41598-017-14455-0.
- [87] G. Liu, X. Cui, and S. Dong, "A tunable ring-type magnetoelectric inductor," *Journal of Applied Physics*, vol. 108, no. 9, 2010/11/01 2010, doi: 10.1063/1.3504218.
- [88] Z. Chu, M. PourhosseiniAsl, and S. Dong, "Review of multi-layered magnetoelectric composite materials and devices applications," *Journal of Physics D: Applied Physics*, vol. 51, no. 24, p. 243001, 2018/05/21 2018, doi: 10.1088/1361-6463/aac29b.
- [89] C. A. F. Vaz, "Electric field control of magnetism in multiferroic heterostructures," *Journal of Physics: Condensed Matter*, vol. 24, no. 33, p. 333201, 2012/07/24 2012, doi: 10.1088/0953-8984/24/33/333201.
- [90] Y. Yan *et al.*, "High-Power Magnetoelectric Voltage Tunable Inductors," *IEEE Transactions on Industrial Electronics*, vol. 68, no. 6, pp. 5355-5365, 2021, doi: 10.1109/TIE.2020.2989719.
- [91] C. Song, B. Cui, F. Li, X. Zhou, and F. Pan, "Recent progress in voltage control of magnetism: Materials, mechanisms, and performance," *Progress in Materials Science*, vol. 87, pp. 33-82, 2017/06/01/2017, doi: <https://doi.org/10.1016/j.pmatsci.2017.02.002>.
- [92] J. Zhang *et al.*, "Theory of tunable magnetoelectric inductors in ferrite-piezoelectric layered composite," *Journal of Physics D: Applied Physics*, vol. 52, no. 16, p. 165001, 2019/02/11 2019, doi: 10.1088/1361-6463/ab01a3.
- [93] P. Švec *et al.*, "Magnetoelastic Properties of Selected Amorphous Systems Tailored by Thermomagnetic Treatment," *Journal of Electrical Engineering*, vol. 65, pp. 259-261, August 01, 2014 2014, doi: 10.2478/jee-2014-0040.
- [94] J. Ou-Yang *et al.*, "Magnetolectric laminate composites: an overview of methods for improving the DC and low-frequency response," *Journal of Physics D: Applied Physics*, vol. 51, no. 32, p. 324005, 2018/07/18 2018, doi: 10.1088/1361-6463/aaced8.
- [95] M. L. Spano, K. B. Hathaway, and H. T. Savage, "Magnetostriction and magnetic anisotropy of field annealed Metglas* 2605 alloys via dc M-H loop measurements under stress," *Journal of Applied Physics*, vol. 53, no. 3, pp. 2667-2669, 1982, doi: 10.1063/1.330932.
- [96] G. Liu, Y. Zhang, P. Ci, and S. Dong, "Enhanced electrical manipulation of magnetic susceptibility in ferromagnetic amorphous alloy and piezoelectric bimorph heterostructure," *Journal of Applied Physics*, vol. 114, no. 6, 2013, doi: 10.1063/1.4817919.
- [97] J. Lou, M. Liu, D. Reed, Y. Ren, and N. X. Sun, "Giant Electric Field Tuning of Magnetism in Novel Multiferroic FeGaB/Lead Zinc Niobate-Lead Titanate (PZN-PT) Heterostructures," *Advanced Materials*, vol. 21, no. 46, pp. 4711-4715, 2009/12/11 2009, doi: <https://doi.org/10.1002/adma.200901131>.
- [98] X. Fang, N. Zhang, and Z. L. Wang, "Converse magnetoelectric effects on heterotype electrostrain-piezopermeability composites," *Appl. Phys. Lett.*, vol. 93, no. 10, p. 102503, 2008/9/8 2008, doi: 10.1063/1.2979699.
- [99] C. Sun *et al.*, "Electrostatically Tunable Mutual Inductance for Frequency Splitting Elimination in Wireless Power Transfer," *IEEE Transactions on Magnetics*, vol. 58, no. 2, pp. 1-6, 2022, doi: 10.1109/TMAG.2021.3132768.
- [100] H. Lin *et al.*, "Voltage Tunable Magnetoelectric Inductors With Improved Operational Frequency and Quality Factor for Power Electronics," *IEEE Transactions on Magnetics*, vol. 51, no. 1, pp. 1-5, 2015, doi: 10.1109/TMAG.2014.2326619.
- [101] D. V. Savelev, L. Y. Fetisov, D. V. Chashin, and Y. K. Fetisov, "Magnetolectric Ring-Type Inductors Tuned by Electric and Magnetic Fields," *IEEE Sensors Letters*, vol. 5, no. 11, pp. 1-4, 2021, doi: 10.1109/LSENS.2021.3119206.
- [102] Y. Yan *et al.*, "Colossal tunability in high frequency magnetoelectric voltage tunable inductors," *Nature Communications*, vol. 9, no. 1, p. 4998, 2018/11/27 2018, doi: 10.1038/s41467-018-07371-y.
- [103] H. Wang, L. Qu, W. Qiao, and B. Liu, "Magnetic Flux Valve: A Magnetoelectric Materials-Based Device for Conversion and Control of Electric Power," *IEEE Transactions on Industrial Electronics*, vol. 64, no. 3, pp. 2451-2458, 2017, doi: 10.1109/TIE.2016.2597759.
- [104] J. Cui, H. Wang, L. Qu, and W. Qiao, "A tunable inductor based on a magnetic flux valve," in *2017 IEEE Energy Conversion Congress and Exposition (ECCE)*, 1-5 Oct. 2017 2017, pp. 3255-3259, doi: 10.1109/ECCE.2017.8096589.
- [105] J. Cui, L. Qu, and W. Qiao, "A Three-Phase Adjustable-Voltage-Ratio Transformer Based on Magnetic Flux Valves," in *2018 IEEE Energy Conversion Congress and Exposition (ECCE)*, 23-27 Sept. 2018 2018, pp. 758-762, doi: 10.1109/ECCE.2018.8558375.
- [106] J. Cui, C. Jia, L. Qu, and W. Qiao, "Analysis and Suppression of Corner Electric Field in Magnetic Flux Valves," in *2021 IEEE Energy Conversion Congress and Exposition (ECCE)*, 10-14 Oct. 2021 2021, pp. 5523-5527, doi: 10.1109/ECCE47101.2021.9595009.
- [107] H. V. Marques, A. R. Seidel, M. S. Perdigão, J. M. Alonso, and E. S. Saraiva, "Constant-Frequency Magnetically Controlled Universal Ballast With SoS Compliance for TL5 Fluorescent Lamps," *IEEE Transactions on Power Electronics*, vol. 27, no. 4, pp. 2163-2175, 2012, doi: 10.1109/TPEL.2011.2165225.
- [108] J. M. Alonso, M. A. Dalla-Costa, J. Cardesín, and J. García, "Magnetic dimming of electronic ballasts," *Electronics Letters*, vol. 41, no. 12, pp. 718-719, [Online]. Available: https://digital-library.theiet.org/content/journals/10.1049/el_20058340
- [109] U. Boeke, "Scalable fluorescent lamp driver using magnetic amplifiers," in *2005 European Conference on Power Electronics and Applications*, 11-14 Sept. 2005 2005, pp. 10 pp.-P.10, doi: 10.1109/EPE.2005.219246.
- [110] J. M. Alonso, M. A. D. Costa, M. Rico-Secades, J. Cardesin, and J. Garcia, "Investigation of a New Control Strategy for Electronic Ballasts Based on Variable Inductor," *IEEE Transactions on Industrial Electronics*, vol. 55, no. 1, pp. 3-10, 2008, doi: 10.1109/TIE.2007.896033.
- [111] S. Borekci, "Dimming Electronic Ballasts Without Striations," *IEEE Transactions on Industrial Electronics*, vol. 56, no. 7, pp. 2464-2468, 2009, doi: 10.1109/TIE.2009.2017561.
- [112] M. S. Perdigão, J. M. Alonso, M. A. D. Costa, and E. S. Saraiva, "Optimization of universal ballasts through magnetic regulators," in *2008 Twenty-Third Annual IEEE Applied Power Electronics Conference and Exposition*, 24-28 Feb. 2008 2008, pp. 1214-1220, doi: 10.1109/APEC.2008.4522877.
- [113] R. A. Pinto, J. M. Alonso, M. S. Perdigão, M. F. d. Silva, and R. N. d. Prado, "A new technique to equalize branch currents in multiarray LED lamps based on variable inductor," in *2014 IEEE Industry Application Society Annual Meeting*, 5-9 Oct. 2014 2014, pp. 1-9, doi: 10.1109/IAS.2014.6978424.
- [114] R. A. Pinto, J. M. Alonso, M. S. Perdigão, M. F. d. Silva, and R. N. d. Prado, "A New Technique to Equalize Branch Currents in Multiarray LED Lamps Based on Variable Inductors," *IEEE Transactions on Industry Applications*, vol. 52, no. 1, pp. 521-530, 2016, doi: 10.1109/TIA.2015.2483596.
- [115] Y. Hu, L. Huber, and M. M. Jovanović, "Universal-input single-stage PFC flyback with variable boost inductance for high-brightness LED applications," in *2010 Twenty-Fifth Annual IEEE Applied Power Electronics Conference and Exposition (APEC)*, 21-25 Feb. 2010 2010, pp. 203-209, doi: 10.1109/APEC.2010.5433669.
- [116] Y. Hu, L. Huber, and M. M. Jovanović, "Single-Stage, Universal-Input AC/DC LED Driver With Current-Controlled Variable PFC Boost Inductor," *IEEE Transactions on Power Electronics*, vol. 27, no. 3, pp. 1579-1588, 2012, doi: 10.1109/TPEL.2010.2082564.
- [117] E. Orietti, P. Mattavelli, G. Spiazzi, C. Adragna, and G. Gattavari, "Two-phase interleaved LLC resonant converter with current-controlled inductor," in *2009 Brazilian Power Electronics Conference*, 27 Sept.-1 Oct. 2009 2009, pp. 298-304, doi: 10.1109/COBEP.2009.5347671.
- [118] J. M. Alonso, M. S. Perdigão, D. Gacio, L. Campa, and E. S. Saraiva, "Magnetic control of DC-DC resonant converters provides constant frequency operation," *Electronics Letters*, vol. 46, no. 6, pp. 440-442, [Online]. Available: <https://digital-library.theiet.org/content/journals/10.1049/el.2010.0191>
- [119] J. M. Alonso, M. S. Perdigão, D. G. Vaquero, A. J. Calleja, and E. S. Saraiva, "Analysis, Design, and Experimentation on Constant-Frequency DC-DC Resonant Converters With Magnetic Control," *IEEE Transactions on Power Electronics*, vol. 27, no. 3, pp. 1369-1382, 2012, doi: 10.1109/TPEL.2011.2165083.
- [120] V. S. Costa, M. S. Perdigão, A. S. Mendes, and J. M. Alonso, "Evaluation of a variable-inductor-controlled LLC resonant converter for battery charging applications," in *IECON 2016 - 42nd Annual Conference of the IEEE Industrial Electronics Society*, 23-26 Oct. 2016 2016, pp. 5633-5638, doi: 10.1109/IECON.2016.7793916.

- [121] Y. Wei, Q. Luo, X. Du, N. Altin, A. Nasiri, and J. M. Alonso, "A Dual Half-Bridge LLC Resonant Converter With Magnetic Control for Battery Charger Application," *IEEE Transactions on Power Electronics*, vol. 35, no. 2, pp. 2196-2207, 2020, doi: 10.1109/TPEL.2019.2922991.
- [122] Y. Wei, N. Altin, Q. Luo, and A. Nasiri, "A High Efficiency, Decoupled On-board Battery Charger with Magnetic Control," in *2018 7th International Conference on Renewable Energy Research and Applications (ICRERA)*, 14-17 Oct. 2018 2018, pp. 920-925, doi: 10.1109/ICRERA.2018.8566835.
- [123] Y. Wei, Q. Luo, Z. Wang, L. Wang, J. Wang, and J. Chen, "Design of LLC Resonant Converter with Magnetic Control for LEV Application," in *2019 IEEE 10th International Symposium on Power Electronics for Distributed Generation Systems (PEDG)*, 3-6 June 2019 2019, pp. 857-862, doi: 10.1109/PEDG.2019.8807637.
- [124] Y. Wei, Q. Luo, X. Du, N. Altin, J. M. Alonso, and H. A. Mantooth, "Analysis and Design of the LLC Resonant Converter With Variable Inductor Control Based on Time-Domain Analysis," *IEEE Transactions on Industrial Electronics*, vol. 67, no. 7, pp. 5432-5443, 2020, doi: 10.1109/TIE.2019.2934085.
- [125] Y. Wei, Q. Luo, S. Chen, Q. He, and L. Zhou, "A High Efficiency Single Stage Bi-directional Battery Charger with Magnetic Control," in *2018 IEEE International Power Electronics and Application Conference and Exposition (PEAC)*, 4-7 Nov. 2018 2018, pp. 1-6, doi: 10.1109/PEAC.2018.8590569.
- [126] Y. Wei, Q. Luo, D. Woldegiorgis, H. Mhiesan, and A. Mantooth, "Analysis of a Magnetically Controlled Single Stage LLC Resonant Converter," in *2020 IEEE Applied Power Electronics Conference and Exposition (APEC)*, 15-19 March 2020 2020, pp. 1257-1263, doi: 10.1109/APEC39645.2020.9124393.
- [127] Y. Wei, Q. Luo, and A. Mantooth, "Comprehensive analysis and design of LLC resonant converter with magnetic control," *CPSS Transactions on Power Electronics and Applications*, vol. 4, no. 4, pp. 265-275, 2019, doi: 10.24295/CPSSTPEA.2019.00025.
- [128] Y. Wei, Q. Luo, D. Woldegiorgis, and A. Mantooth, "Multiple-Output LLC Resonant Converter with Magnetic Control," in *2020 IEEE Energy Conversion Congress and Exposition (ECCE)*, 11-15 Oct. 2020 2020, pp. 1204-1209, doi: 10.1109/ECCE44975.2020.9235791.
- [129] Y. Wei, Q. Luo, J. Wang, and S. Pengju, "Analysis and design of the DCM operation boost PFC converter with magnetic control," *IET Power Electronics*, vol. 12, no. 14, pp. 3697-3706, 2019, doi: <https://doi.org/10.1049/iet-pel.2019.0437>.
- [130] S. Saeed and J. Garcia, "Extended Operational Range of Dual-Active-Bridge Converters by using Variable Magnetic Devices," in *2019 IEEE Applied Power Electronics Conference and Exposition (APEC)*, 17-21 March 2019 2019, pp. 1629-1634, doi: 10.1109/APEC.2019.8721920.
- [131] S. Saeed, J. Garcia, M. S. Perdigão, V. S. Costa, and R. Georgious, "Evaluation of temperature effect on inductance computation in variable magnetic components for Dual-Active-Bridge application," in *2020 IEEE Energy Conversion Congress and Exposition (ECCE)*, 11-15 Oct. 2020 2020, pp. 3286-3292, doi: 10.1109/ECCE44975.2020.9236197.
- [132] J. u. W. Hsu, A. P. Hu, A. Swain, X. Dai, and Y. Sun, "A new contactless power pick-up with continuous variable inductor control using magnetic amplifier," in *2006 International Conference on Power System Technology*, 22-26 Oct. 2006 2006, pp. 1-8, doi: 10.1109/ICPST.2006.321556.
- [133] J. U. W. Hsu and A. P. Hu, "Determining the variable inductance range for an LCL wireless power pick-up," in *2007 IEEE Conference on Electron Devices and Solid-State Circuits*, 20-22 Dec. 2007 2007, pp. 489-492, doi: 10.1109/EDSSC.2007.4450169.
- [134] S. Aldhaher, P. C. K. Luk, and J. F. Whidborne, "Electronic Tuning of Misaligned Coils in Wireless Power Transfer Systems," *IEEE Transactions on Power Electronics*, vol. 29, no. 11, pp. 5975-5982, 2014, doi: 10.1109/TPEL.2014.2297993.
- [135] V. S. Meshram, F. Corti, L. Solimene, S. Musumeci, C. S. Ragusa, and A. Reatti, "Variable Inductor Control Strategy in LCC-S Compensated Wireless Power Transfer Application," in *2023 AEIT International Annual Conference (AEIT)*, 5-7 Oct. 2023 2023, pp. 1-6, doi: 10.23919/AEIT60520.2023.10330337.
- [136] C. Li et al., "Variable-Inductor Based Tuning Method for Multiple-Relay Wireless Power Transfer System in Composite Insulator," in *2023 5th Asia Energy and Electrical Engineering Symposium (AEEES)*, 23-26 March 2023 2023, pp. 390-395, doi: 10.1109/AEEES56888.2023.10114074.
- [137] J. Zhao, Y. Zhang, and L. Qi, "Design and Analysis of a Flexible Multi-Output Wireless Power Transfer System with Variable Inductor," in *2021 IEEE Energy Conversion Congress and Exposition (ECCE)*, 10-14 Oct. 2021 2021, pp. 1559-1564, doi: 10.1109/ECCE47101.2021.9595052.
- [138] L. Solimene, F. Corti, S. Musumeci, C. S. Ragusa, and A. Reatti, "Magnetic Control of LCC-S Compensated Wireless Power Transfer System," in *2022 International Symposium on Power Electronics, Electrical Drives, Automation and Motion (SPEEDAM)*, 22-24 June 2022 2022, pp. 160-165, doi: 10.1109/SPEEDAM53979.2022.9842241.
- [139] M. Xianmin, Z. Suli, W. Jianze, and J. Yanchao, "Novel Static Var Compensator Based on Ferrite Orthogonal Core Controlled Reactor," in *2006 IEEE International Conference on Industrial Technology*, 15-17 Dec. 2006 2006, pp. 1903-1907, doi: 10.1109/ICIT.2006.372538.
- [140] M. Xianmin, W. Jianze, J. Yanchao, W. Xiaoxia, and F. Xiangyun, "Novel Harmonic Free Single Phase Variable Inductor Based on Active Power Filter Strategy," in *2006 CES/IEEE 5th International Power Electronics and Motion Control Conference*, 14-16 Aug. 2006 2006, vol. 3, pp. 1-4, doi: 10.1109/IPEMC.2006.4778289.
- [141] A. A. Huzayyin, "Utilizing the nonlinearity of a magnetic core inductor as a source of variable reactive power compensation in electric power systems," in *2008 Annual IEEE Student Paper Conference*, 15-26 Feb. 2008 2008, pp. 1-4, doi: 10.1109/AISPC.2008.4460569.
- [142] L. Zhang, W. G. Hurley, and W. Wölflle, "A new approach to achieve maximum power point tracking for PV system with a variable inductor," in *The 2nd International Symposium on Power Electronics for Distributed Generation Systems*, 16-18 June 2010 2010, pp. 948-952, doi: 10.1109/PEDG.2010.5545758.
- [143] L. Zhang, W. G. Hurley, and W. H. Wölflle, "A New Approach to Achieve Maximum Power Point Tracking for PV System With a Variable Inductor," *IEEE Transactions on Power Electronics*, vol. 26, no. 4, pp. 1031-1037, 2011, doi: 10.1109/TPEL.2010.2089644.
- [144] Y. K. E. Ho, S. T. S. Lee, H. S. H. Chung, and S. Y. Hui, "A comparative study on dimming control methods for electronic ballasts," *IEEE Transactions on Power Electronics*, vol. 16, no. 6, pp. 828-836, 2001, doi: 10.1109/63.974381.
- [145] Z. He, G. Zhang, Z. Chen, and S. S. Yu, "A Review of Variable-inductor-based Power Converters for Eco-friendly Applications: Fundamentals, Configurations, and Applications," *Chinese Journal of Electrical Engineering*, vol. 9, no. 3, pp. 50-71, 2023, doi: 10.23919/CJEE.2023.000030.
- [146] S. Y. R. Hui, L. Leung Ming, H. S. H. Chung, and Y. K. Ho, "An electronic ballast with wide dimming range, high PF, and low EMI," *IEEE Transactions on Power Electronics*, vol. 16, no. 4, pp. 465-472, 2001, doi: 10.1109/63.931047.
- [147] M. S. Perdigão, M. Menke, A. R. Seidel, R. A. Pinto, and J. M. Alonso, "A review on variable inductors and variable transformers: Applications to lighting drivers," in *2014 IEEE Industry Application Society Annual Meeting*, 5-9 Oct. 2014 2014, pp. 1-8, doi: 10.1109/IAS.2014.6978431.
- [148] S. Li, S. C. Tan, C. K. Lee, E. Waffenschmidt, S. Y. Hui, and C. K. Tse, "A survey, classification, and critical review of light-emitting diode drivers," *IEEE Transactions on Power Electronics*, vol. 31, no. 2, pp. 1503-1516, 2016, doi: 10.1109/TPEL.2015.2417563.
- [149] Electromagnetic compatibility (EMC), Part 3-2: Limits - Limits for harmonic current emissions (equipment input current $\leq 16\text{ A}$ per phase), IEC 61000-3-2, I. E. Commission, 2018.
- [150] Y. Hu, L. Huber, and M. M. Jovanovic, "Single-Stage Flyback Power-Factor-Correction Front-End for HB LED Application," in *2009 IEEE Industry Applications Society Annual Meeting*, 4-8 Oct. 2009 2009, pp. 1-8, doi: 10.1109/IAS.2009.5324874.

Highlights

- Actively-controlled variable inductors are widely employed in power electronic converters.
- Current-controlled variable inductors have proven to improve power electronic converters' performance.
- Current-controlled variable inductors were extensively employed in lighting drivers, resonant converters, and inductive wireless power transmission.
- Current-controlled variable inductors have been utilized in dual-active-bridge converters for improving converter's efficiency.
- Voltage-controlled variable inductors are more compact and efficient than current-controlled ones, yet they are seldom used due to their expensive cost.

Author's Biography



Raheem Elsayed was born in Minya Al-Qamh, Al-Sharqiyyah, Egypt, in 1997. In 2020, he received his B.Sc. degree in electrical power systems and machine engineering from Zagazig University in Al-Sharqiyyah, Egypt. Currently, he serves as a teaching and research assistant at the department of electrical power systems and machines at Zagazig University. His current research interests focus on power electronics for renewable energy systems, power electronics for aircraft applications, and magnetics for power electronics. Mr. Raheem is a member of the IEEE, the IEEE Power Electronics Society, the IEEE Power and Energy Society, and the IEEE Industry Applications Society.